JOURNAL OF GEOPHYSICAL RESEARCH, VOL. 106, NO. B11, PAGES 26,541–26,560, NOVEMBER 10, 2001

Viscoelastic shear zone model of a strike-slip earthquake cycle

Fred F. Pollitz[1]

Department of Geology, University of California, Davis, California, USA

Abstract. I examine the behavior of a two-dimensional (2-D) strike-slip fault system embedded in a 1-D elastic layer (schizosphere) overlying a uniform viscoelastic half-space (plastosphere) and within the boundaries of a finite width shear zone. The viscoelastic coupling model of *Savage and Prescott* [1978] considers the viscoelastic response of this system, in the absence of the shear zone boundaries, to an earthquake occurring within the upper elastic layer, steady slip beneath a prescribed depth, and the superposition of the responses of multiple earthquakes with characteristic slip occurring at regular intervals. So formulated, the viscoelastic coupling model predicts that sufficiently long after initiation of the system, (1) average fault-parallel velocity at any point is the average slip rate of that side of the fault and (2) far-field velocities equal the same constant rate. Because of the sensitivity to the mechanical properties of the schizosphere-plastosphere system (i.e., elastic layer thickness, plastosphere viscosity), this model has been used to infer such properties from measurements of interseismic velocity. Such inferences exploit the predicted behavior at a known time within the earthquake cycle. By modifying the viscoelastic coupling model to satisfy the additional constraint that the absolute velocity at prescribed shear zone boundaries is constant, I find that even though the time-averaged behavior remains the same, the spatiotemporal pattern of surface deformation (particularly its temporal variation within an earthquake cycle) is markedly different from that predicted by the conventional viscoelastic coupling model. These differences are magnified as plastosphere viscosity is reduced or as the recurrence interval of periodic earthquakes is lengthened. Application to the interseismic velocity field along the Mojave section of the San Andreas fault suggests that the region behaves mechanically like a ~600-km-wide shear zone accommodating 50 mm/yr fault-parallel motion distributed between the San Andreas fault system and Eastern California Shear Zone.

1. Introduction

In the viscoelastic coupling model [*Savage and Prescott*, 1978], time-dependent deformation around a strike-slip fault zone is realized by loading, subsequent rupture, and relaxation of a fault present in a schizosphere (elastic upper crust) overlying a ductile plastosphere. Assuming a two-dimensional (2-D) geometry, periodic rupture of the fault, and identical slip, interseismic deformation is obtained as the superposition of viscoelastic relaxation of the plastosphere summed over the infinity of past periodic earthquakes. This model yields far-field interseismic motions equal to $\pm$ 1/2 of the average slip rate v_0 imposed on the fault. Thus, even when no external mechanism is invoked to load the fault (i.e., when the locked portion of the fault penetrates the entire schizosphere), the model satisfies the expectation of rigid plate-like behavior in the far field. In addition, when periodic coseismic offsets are factored in, the model predicts that the time-averaged fault-parallel velocity of each point is $\pm v_0/2$ (depending on location).

The viscoelastic coupling model makes specific predictions for interseismic velocities near the fault as well. In particular, it predicts a wide range of variation in interseismic velocity depending on observation time since the last characteristic event, Maxwell relaxation time of the plastosphere $2\eta/\mu$ (where η is viscosity and μ is shear modulus), and time interval T between repeated earthquakes. In general, fault-parallel velocity diminishes with time into the cycle. Moreover, when the Maxwell relaxation time is small compared with T, fault-parallel velocity near the fault will exceed $v_0/2$ at short times after the last earthquake but be considerably less than $v_0/2$ near the end of the cycle. The spatial velocity patterns produced during a cycle are generally broader than would be expected from a secular strain accumulation model prescribed by aseismic slip on a vertical plane beneath the seismogenic layer. In southern California around the Mojave segment of the San Andreas fault (SAF) the interseismic velocity and strain fields as constrained by trilateration [*Ebertart-Phillips et al.*, 1990; *Savage and Lisowski*, 1998] and combined triangulation, trilateration, and GPS [*Shen et al.*, 1996] are well described in terms of strain accumulation on the deep vertical extension of the SAF with an apparent locking depth of ~30 km. The seismogenic layer is only 12-18 km thick in this area [*Webb and Kanamori*, 1985; *Jones*, 1988; *Hill et al.*, 1990], and locking depths greater than this should not be expected. *Shen et al.* [1996] have shown that the velocity field cannot be explained even with a reasonable distribution of deep dislocations beneath the SAF and nearby parallel faults using shallower locking depths ~15 km. *Savage and Lisowski* [1998] encountered the same problem when interpreting trilateration data very close to the SAF, and they resolved it by interpreting

[1]Now at U.S. Geological Survey, Menlo Park, California, USA

Paper number 2001JB000342
0148-0227/01/2001JB000342$09.00

the apparently large locking depth in terms of the viscoelastic coupling model which prescribes a reasonable thickness (10–15 km) for the schizosphere.

The success of the viscoelastic coupling model for modeling the near-fault data considered by *Savage and Lisowski* [1998] suggests that it should be applicable to the long velocity profile across the Mojave section of the SAF obtained by *Shen et al.* [1996] and should help to resolve the issue of apparently large locking depth. At larger distances from the SAF, however, the model encounters a difficulty: predicted fault-parallel velocity at large (but not infinite, i.e., ~500 km) distance from the SAF fault reaches only a fraction of the long-term velocity on each side of the fault at intermediate to late times during the earthquake cycle. The model predicts small but significant horizontal strains even beyond such distances, integrating over a large horizontal length scale in order to complete the budget of long-term slip rate and to produce plate-like behavior in the far field. As such, this model excludes the possibility that a continental shear zone be bounded by blocks which are relatively thick and nondeforming. For example, the Sierra Nevada block, which bounds both the northern SAF system and Eastern California Shear Zone, possesses these properties, based on both seismic tomography [*Humphreys and Dueker*, 1994] and geodetic measurements [*Dixon et al.*, 2000]. Oceanic lithosphere also possesses these properties [*Brace and Kohlstedt*, 1980] and controls to a large extent the history of continental deformation within the well-developed strike-slip fault systems in California [*Atwater and Stock*, 1998] and Turkey [*McClusky et al.*, 2000]. Around the southern SAF system itself, very long baseline interferometry (VLBI) data collected in the 1980s and 1990s [*Gordon et al.*, 1993] reveal that most of the Pacific to North America relative plate motion is accommodated in a roughly 600 to 1000-km-wide zone. The viscoelastic coupling model thus goes a long way towards resolving the existence of broad zones of strain accumulation under the condition that the seismogenic zone be restricted in depth, but it appears incompatible with the accommodation of most of the relative plate motion within a broad, but finite-width, zone as well as the existence of relatively nondeforming blocks around this zone.

An alternative framework designed to accommodate plate-like behavior at the boundaries of a broad shear zone postulates that (1) viscoelastic relaxation from a quasi-cyclic history of great earthquakes and (2) loading of a finite-width shear zone contribute in varying degrees to presently observed interseismic deformation. In this conceptual model a shear zone loads faults from the side, stresses accumulating on the faults may be accommodated by steady creep (full or partial) at any depth level in the schizosphere or plastosphere, and earthquakes occur periodically to relieve the stresses on the locked portions of the faults. Other integrated models have been proposed, notably combined viscoelastic relaxation, basal shear, and shear zone loading [*Roy and Royden*, 2000a, 2000b]. The net effect of factoring in external sources of fault loading is that the time history of any point near the fault is more uniform; that is, the large excursions in velocity between the early and late cycle times are reduced, and plate-like behavior is satisfied at a certain distance from the fault. In the following, I concentrate on the steps necessary to append the viscoelastic coupling model of *Savage and Prescott* [1978] with loading of a finite width shear zone. I will then conduct an analysis of the interseismic velocity field around the Mojave segment of the SAF to illustrate the applicability of the viscoelastic shear zone model to recent measurements.

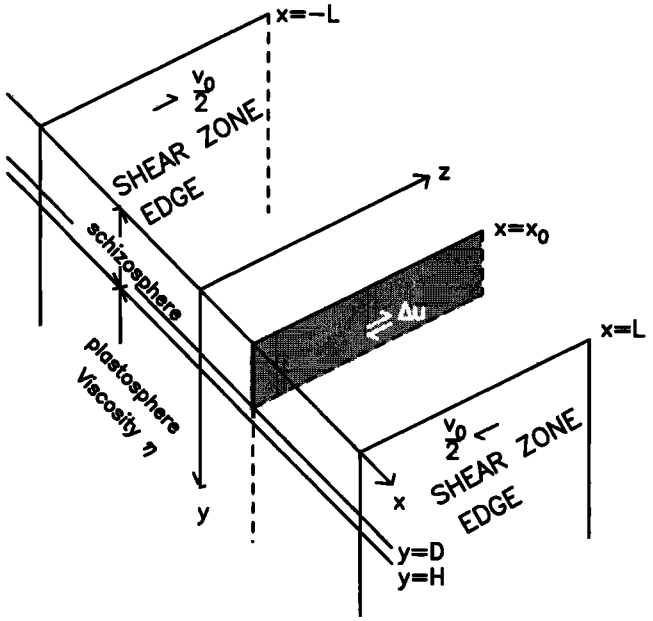

Figure 1. Geometry of strike-slip faulting. A fault parallel to the z–axis at $x = x_0$ and extending from $y = 0$ to $y = D$ (shaded region) is embedded in an elastic schizosphere of thickness H. This is underlain by a Maxwell viscoelastic plastosphere of viscosity η. This laterally homogeneous model (viscoelastic coupling model) is subjected to constant velocity boundary conditions at the walls of shear zone ($x = \pm L$) to produce the viscoelastic shear zone model. At the end of one elementary earthquake cycle the fault slips with magnitude Δu.

2. Development

2.1. Two-Dimensional Shear Zone Deformation

I assume an $x - y - z$ Cartesian geometry with x the distance from a vertical fault, y the depth coordinate, and z the fault-parallel distance (Figure 1). A shear zone of width $2L$ encompasses a fault located at $x = x_0$ ($-L < x_0 < L$). The fault is taken infinitely long, so that the problem becomes two-dimensional. The velocity $v = \partial_t u_z$ at $x = \pm L$ is taken to be $\pm v_0/2$ at all times, regardless of depth; that is, the shear zone accommodates a relative plate motion of v_0 between the two bounding blocks. It is an approximation to the process of strain accumulation and release in a laterally variable viscoelastic system in which the plastosphere occupying the shear zone is much weaker than the plastosphere outside of it. Since all sources of deformation to be considered here will be transient (earthquake-related) sources, I will consider the deformation produced by fault motion such that the shear zone boundaries are displacement-free. The total velocity would then be a superposition of the transient deformation plus secular simple shear across the shear zone.

Our solution will be constructed from the solutions of the equations of static equilibrium in an elastic half-space whose material properties may vary in the x and y directions but not in the z direction. Consider the solution $\mathbf{u}(x,y)$ of the equations

$$\nabla\cdot\mathbf{T} = -\mathbf{M}:\nabla\delta(x - x_0,y_0) \quad (1)$$

$$\mathbf{T} = \lambda(\nabla\cdot\mathbf{u})\,\mathbf{I} + 2\mu\varepsilon, \tag{2}$$

where $\mathbf{M}$ is the moment tensor, $\mathbf{T}$ is the stress tensor, $\mathbf{I}$ is the identity matrix, λ and μ are the Lame parameters, and ε is the strain tensor:

$$\varepsilon = \frac{1}{2}\left[\nabla\mathbf{u} + (\nabla\mathbf{u})^T\right]. \tag{3}$$

Particular solutions $\mathbf{u} = \mathbf{u}_0$ of (1)-(3) for the case x_0=0 are solved subject to the conditions that $\lim_{x\to\infty}\mathbf{u}_0(x,y)$ and $\lim_{y\to\infty}\mathbf{u}_0(x,y)$ exist and are finite and that $\mathbf{u}_0$ obeys the symmetry

$$\mathbf{u}_0(-x,y) = -\mathbf{u}_0(x,y). \tag{4}$$

Condition (4) will be satisfied for any $\mathbf{M}$ corresponding to a shear dislocation on the plane $x = 0$; i.e., a combination of pure dip-slip and pure strike-slip motion on the fault plane. We restrict attention to only the case of strike-slip motions.

Solutions of (1)-(3) are well known for both a uniform elastic half-space and stratified elastic media, with solutions readily obtained by means of the Betti reciprocity theorem [*Savage*, 1980] or propagator matrix methods [e.g., *Wason and Singh*, 1972; *Rundle*, 1980].

In the viscoelastic shear zone model I seek the solutions to (1)-(3) subject to different boundary conditions. For a sufficiently wide shear zone, coseismic offsets at the shear zone edges will comprise a very small portion of the slip budget, and the velocity at those edges during interseismic periods will be approximately constant. Thus it is appropriate to impose the boundary condition

$$\mathbf{u}(L,y) = \mathbf{u}(-L,y) = 0. \tag{5}$$

Consider first the case where the fault plane bisects the shear zone: $x_0 = 0$. Solutions to (1)-(3) subject to (5) may be constructed from particular solutions $\mathbf{u}_0$ by means of superposition of successive image solutions:

$$\mathbf{u}(x,y) = \mathbf{u}_0(x,y) + \sum_{N=1}^{\infty}\left[\mathbf{u}_0(x+2LN,y) + \mathbf{u}_0(x-2LN,y)\right] - \left[\lim_{x\to\infty}\mathbf{u}_0(x,y)\right]\frac{x}{L}\quad(-L \le x \le L, y \ge 0). \tag{6}$$

This consists of a superposition of the original source at $x = 0$ plus image sources located at $x = \pm 2L$, $4L$, $6L$, etc., plus simple shear. Since each image source and the solution x/L satisfy the homogeneous system (1)-(3) (i.e., without the source term), it follows from (4) that $\mathbf{u}(\pm L, y)$ converge to zero.

Consider next the more general case $-L < x_0 < L$ (the fault plane not necessarily bisecting the shear zone). The solution is

$$\mathbf{u}(x,y) = \mathbf{u}_0(x-x_0,y) + \sum_{m=1}^{\infty}\left\{\mathbf{u}_0[x+(2L)(2m)-x_0,y] + \mathbf{u}_0[x-(2L)(2m)-x_0,y]\right\} + \sum_{m=1}^{\infty}\left\{\mathbf{u}_0[x+2L(2m-1)+x_0,y] + \mathbf{u}_0[x-2L(2m-1)+x_0,y]\right\} - \left[\lim_{x\to\infty}\mathbf{u}_0(x,y)\right]\frac{x}{L}. \tag{7}$$

This consists of a superposition of the original source at $x = x_0$ plus image sources located at $x = 2L-x_0$, $4L+x_0$, $6L-x_0$, $10L+x_0$,... and $x = -2L-x_0$, $-4L+x_0$, $-6L-x_0$, $-10L+x_0$, etc., plus a simple shear. It is clear that the two m summations in (7) span the range of even and odd integer multiples of $2L$, respectively.

Solutions (6) and (7) are, of course, applicable not only to single solutions of (1)-(3) but also to linear combinations of these solutions. In particular, they are applicable to describe time-evolving viscoelastic deformation associated with steady or step-like elastic dislocations in situations which satisfy the 2-D geometry and the linear stress-strain relation (2). In the following sections we obtain expressions for time-dependent deformation associated with specific dislocations on a laterally homogeneous viscoelastic Earth model, derive the modification to this deformation in the presence of the shear zone, and explore general implications for the behavior of a strike-slip fault system constrained by a shear zone.

2.2. Viscoelastic Coupling Model

Following *Savage and Prescott* [1978], I outline the solution for time-dependent deformation at Earth's surface associated with a strike-slip dislocation, assuming the 2-D geometry of Figure 1. Throughout our analysis, the only nontrivial displacement component is that parallel to the z axis. A vertical fault taken parallel to the z-axis extends from Earth's surface y=0 to a depth y=D. This is embedded in an elastic layer of thickness H and rigidity μ_1 overlying an elastic half-space of rigidity μ_2. To obtain the elastic response to an earthquake on this fault, we first consider the deformation associated with a dislocation Δu on the vertical plane $y > D$. This is described by a Burgers vector Δu (screw dislocation) applied at y=D. We associate positive Δu to slip below depth D in the left-lateral sense. The elastic solution for z-displacement at Earth's surface is [*Nur and Mavko*, 1974]:

$$u_{Dis}(x,0;t) = \frac{\Delta u(t)}{\pi}\left\{\tan^{-1}\left[\frac{x}{D}\right] + \sum_{n=1}^{\infty}\Gamma^n \cdot\left[\tan^{-1}\left[\frac{x}{2nH+D}\right] - \tan^{-1}\left[\frac{x}{2nH-D}\right]\right]\right\}, \tag{8}$$

where

$$\Gamma = \frac{\mu_1 - \mu_2}{\mu_1 + \mu_2}. \tag{9}$$

We introduce viscoelasticity by allowing the half-space to be viscoelastic with short-term rigidity μ_2^e and viscosity η. We assume that the short-term rigidities of the upper layer and the half-space are identical:

$$\mu_1^e = \mu_2^e = \mu. \tag{10}$$

Viscoelastic deformation is realized by applying the correspondence principle to (1) to obtain $u_{Dis}(x,0;s)$ in the Laplace transform domain, followed by evaluation of the inverse Laplace transform. This requires that $\Delta u(t)$ be replaced by $\Delta u(s) = L[\Delta u(t)]$, and that the rigidity of the half-space be replaced by

$$\mu_2(s) = \frac{\mu\, s}{s + \frac{\mu}{\eta}}. \tag{11}$$

Substituting (10) and (11) into (9) yields

$$\Gamma(s) = \frac{\mu}{2\eta}\,\frac{1}{s + \frac{\mu}{\eta}}. \tag{12}$$

The Laplace-transformed displacement is thus

$$u_{\mathrm{Dis}}(x,0;s) = \frac{\Delta u(s)}{\pi}\left\{\tan^{-1}\left[\frac{x}{D}\right] + \sum_{n=1}^{\infty}[\Gamma(s)]^n \cdot\left[\tan^{-1}\left[\frac{x}{2nH+D}\right] - \tan^{-1}\left[\frac{x}{2nH-D}\right]\right]\right\}. \quad (13)$$

For specific time-dependent dislocations $\Delta u(t)$, time-dependent deformation in the viscoelastic system is obtained by evaluating $L^{-1}[u_{\mathrm{Dis}}(x,0;s)]$. This evaluation requires us to make use of the property

$$L^{-1}\left\{[\Gamma(s)]^n\right\} = \frac{\mu}{2\eta}\,\tau^{n-1}\,e^{-\tau}\,\frac{1}{(n-1)!}, \quad (14)$$

where

$$\tau = \frac{\mu}{2\eta}\,t. \quad (15)$$

We consider two specific source cases. First, we seek the response of the viscoelastic system to an earthquake with left-lateral strike-slip displacement Δu across the vertical plane at $x=0$ from Earth's surface to a depth D. Denoting this response by $u^{(1)}$ we have

$$u^{(1)}(x,0;s) = \frac{\Delta u(s)}{\pi}\left[\pm\frac{\pi}{2}\right] - u_{\mathrm{Dis}}(x,0;s) \quad (16)$$

with $\pm$ taken according to $x \gtrless 0$ and

$$\Delta u(s) = \frac{\Delta u}{s} \quad (17)$$

for a step function source $\Delta u(t) = \Delta u\,H(t)$. In the time domain, from (13)-(16) we obtain

$$u^{(1)}(x,0;t) = \frac{\Delta u}{\pi}\left\{\left[\pm\frac{\pi}{2} - \tan^{-1}\left[\frac{x}{D}\right]\right] - \sum_{n=1}^{\infty} A_n(\tau) \cdot\left[\tan^{-1}\left[\frac{x}{2nH+D}\right] - \tan^{-1}\left[\frac{x}{2nH-D}\right]\right]\right\}$$

$$(t \geq 0) \quad (18)$$

where

$$A_n = \int_0^{\tau} \tau^{n-1}\,e^{-\tau}\,d\tau\,\frac{1}{(n-1)!}. \quad (19)$$

Second, we seek the response of the viscoelastic system to steady slip at a rate v_f below depth D beginning at initial time $t=0$. Denoting this response by $u^{(2)}$, we have

$$u^{(2)}(x,0;s) = u_{\mathrm{Dis}}(x,0;s) \quad (20)$$

with

$$\Delta u(s) = \frac{1}{s^2}\,v_f \quad (21)$$

for a source $\Delta u(t) = v_f\,t \quad (t \geq 0)$. This leads to

$$L^{-1}[\partial_t^2 u^{(2)}(x,0;t)] = \frac{v_f}{\pi}\left\{\tan^{-1}\left[\frac{x}{D}\right] + \sum_{n=1}^{\infty}[\Gamma(s)]^n \cdot\left[\tan^{-1}\left[\frac{x}{2nH+D}\right] - \tan^{-1}\left[\frac{x}{2nH-D}\right]\right]\right\}. \quad (22)$$

Evaluation of the inverse Laplace transform of (22) followed by double integration over time yields

$$u^{(2)}(x,0;t) = \frac{v_f}{\pi}\left\{\left[\tan^{-1}\left[\frac{x}{D}\right]\right]t + \frac{2\eta}{\mu}\sum_{n=1}^{\infty} C_n(\tau) \cdot\left[\tan^{-1}\left[\frac{x}{2nH+D}\right] - \tan^{-1}\left[\frac{x}{2nH-D}\right]\right]\right\}. \quad (23)$$

In deriving (23) we have made use of the relation

$$C_n(\tau) = \int_0^{\tau} A_n(\tau)\,d\tau = \tau\,A_n(\tau) - n\,A_{n+1}(\tau). \quad (24)$$

$A_n(\tau)$ and C_n may be calculated recursively using the relations

$$A_n(\tau) = -\frac{\tau^{n-1}}{(n-1)!}\,e^{-\tau} + A_{n-1}(\tau), \qquad C_n(\tau) = C_{n-1}(\tau) - A_n(\tau), \quad (25)$$

$$A_1(\tau) = 1 - e^{-\tau}, \qquad C_1(\tau) = \tau - A_1(\tau). \quad (26)$$

Equations (25) and (26) are equivalent to equations (20)-(23) of *Savage and Prescott* [1978].

Equations (18) and (23) are the basis for the viscoelastic coupling model of *Savage and Prescott* [1978]. They are convenient for describing the response at Earth's surface from single earthquakes and steady loading, as well as the composite effects of multiple earthquakes compounded over multiple earthquake cycles. In section 2.3 we use these equations as the starting point for generating the viscoelastic response under the boundary conditions appropriate for a finite width shear zone.

2.3. Viscoelastic Shear Zone Model

I examine how the viscoelastic coupling model is modified to account for the effect of embedding the system in a finite width shear zone, also allowing for an arbitrary fault location with respect to the shear zone edges. As written in (7), the required modifications can be obtained in terms of the solution $\mathbf{u}_0$ of the equivalent laterally homogeneous problem by superposition of an infinite series of image sources. The shear zone solution for the two dislocation cases discussed in section 2.2 is obtained by substituting a deformation field of the form $\mathbf{u}_0 = u^{(1)}\,\hat{\mathbf{z}}$ or $\mathbf{u}_0 = u^{(2)}\,\hat{\mathbf{z}}$ (equations (18) or (23)) into (7).

The mathematical form of the image solution (7), involving constant velocity boundary conditions at the shear zone edges, is an approximation which supposes that conditions are appropriate for its validity. Specifically, it is assumed that the shear zone edges as well as the image faults are far removed from the embedded shallow fault(s) such that coseismic offsets from an elastic dislocation along the fault(s) are negligible, i.e., $|x_0 \mp L| \gg H \geq D$. This justifies application of the image solution to the "coseismic" part of the viscoelastic coupling solutions, i.e., the leading terms of (18) and (23). In order to apply the image solution to the "relaxation" parts of (18) and (23) it is further assumed that in the real system, plastosphere viscosity is much lower within the shear zone than outside of it. This may be regarded as assuming that the effective elastic plate thickness is much greater outside of the shear zone than within it. Under partial or complete relaxation of this system the thin stress guide (within the shear zone) does not significantly deform the thick stress guide (bounding material outside of the shear zone) beyond a narrow vertical boundary

layer. These assumptions and conceptual model, made here to justify application of the image solution (7) to a layered viscoelastic system, are also implicit in numerical models that characterize the response of a layered viscoelastic system embedded in a shear zone with plate-like boundary conditions [*Roy and Royden*, 2000a, 2000b]. The accuracy of the approximation is addressed in section 3.5.

It is convenient to define a Greens function $G(x;x_0,L,h)$ as the response of the viscoelastic system, embedded in the shear zone of width $2L$, to a unit Burgers vector applied at position x_0 $(-L < x_0 < L)$ and depth h. This Greens function is derived in Appendix A. The viscoelastic response of the two slip cases considered in section 2.2 can then be evaluated under the shear zone boundary conditions (5) by the expedient of substituting

$$\pm \frac{\pi}{2} \rightarrow \pm \frac{\pi}{2} - \frac{\pi}{2} \frac{x}{L}$$
$$\tan^{-1}\left[\frac{x}{h}\right] \rightarrow G(x;x_0,L,h) \tag{27}$$

throughout equations (18) and (23). For reference I summarize the displacement fields in the viscoelastic shear zone model as follows:

1. Viscoelastic response to an earthquake with left-lateral strike-slip displacement Δu across the vertical plane $x = x_0$ from Earth's surface to depth D is:

$$u_{SZ}^{(1)}(x,0;t) = \frac{\Delta u}{\pi}\left\{\left[\pm\frac{\pi}{2} - \frac{\pi}{2}\frac{x}{L} - G(x;x_0,L,D)\right] - \sum_{n=1}^{\infty} A_n(\tau)\left[G(x;x_0,L,2nH+D) - G(x;x_0,L,2nH-D)\right]\right\}$$
$$(t \geq 0). \tag{28}$$

The $\pm$ sign is taken according to $x \gtrless x_0$.

2. Viscoelastic response to steady slip at a rate v_f on the portion of the vertical plane $x = x_0$ below depth D beginning at initial time $t=0$ is:

$$u_{SZ}^{(2)}(x,0;t) = \frac{v_f}{\pi}\left\{G(x;x_0,L,D)\, t + \frac{2\eta}{\mu}\sum_{n=1}^{\infty} C_n(\tau) \cdot \left[G(x;x_0,L,2nH+D) - G(x;x_0,L,2nH-D)\right]\right\}. \tag{29}$$

The subscript SZ has been used to distinguish the "shear zone" solutions (28)-(29) from the corresponding laterally homogeneous solutions (18) and (23).

The Greens function in (A6) has the property

$$G(\pm L;x_0,L,h) = 0. \tag{30}$$

It follows that each of the shear zone solutions (28) and (29) satisfy the zero-displacement boundary condition (5):

$$u_{SZ}^{(1)}(\pm L,0;t) = u_{SZ}^{(2)}(\pm L,0;t) = 0. \tag{31}$$

3. Shear Zone Response to Earthquake Cycle

3.1. Asymptotic Properties of Conventional Viscoelastic Coupling Model

In the conventional viscoelastic coupling model, steady slip below depth H has vanishingly small effect on surface velocity as $t \rightarrow \infty$. This can be seen be setting $D = H$ and taking the limit $\tau \rightarrow \infty$ in (23). Since

$$\lim_{\tau\rightarrow\infty} A_n(\tau) = 1 \tag{32}$$

$$\partial_t\, C_n(\tau) = \frac{\mu}{2\eta} A_n(\tau), \tag{33}$$

the n-summation in (23) annihilates successive terms, and the remainder after the first n summations approaches

$$\lim_{t\rightarrow\infty} \partial_t u^{(2)}(x,0;t) \sim \tan^{-1}\left[\frac{x}{2(n+1)H}\right] \tag{34}$$

which approaches zero as $n \rightarrow \infty$. The independence of fault-parallel velocity from steady slip in the plastosphere at sufficiently long time after initiation has been proven for other cases of imposed flow in the plastosphere by *Savage* [2000].

We define an elementary earthquake cycle as an interval of steady slip beneath depth D at rate v_f of duration T followed by an earthquake of slip $\Delta u = v_f\, T$ on the fault $(0 < y < D)$. We consider the asymptotic behavior of the viscoelastic system observed a time t $(0 < t \leq T)$ after M consecutive earthquake cycles as $M \rightarrow \infty$.

The velocity in the viscoelastic coupling model at time t after the Mth cycle is

$$v(x,0;t;M) = \left\{\sum_{m=1}^{M} \partial_t u^{(1)}[x,0;t+(m-1)T]\right\} + \partial_t u^{(2)}(x,0;t+MT). \tag{35}$$

(In cycle $M=0$ the term in braces in (35) does not contribute.) Applying the relation

$$\int_0^{\tau_0}\left\{\sum_{m=0}^{M} \partial_t f[\tau + (m-1)\,\tau_0]\right\} d\tau = \frac{\mu}{2\eta} f(\tau + (M-1)\,\tau_0) \tag{36}$$

to

$$f(\tau) = u^{(1)}(x,0;t)$$
$$\tau_0 = \frac{\mu}{2\eta} T, \tag{37}$$

we obtain for the average velocity during the $(M+1)$th cycle (including the earthquake which terminates the cycle):

$$\frac{1}{T}\int_0^T v(x,0;t;M)\, dt = \pm\frac{v_f}{2} + \frac{v_f}{\pi}\sum_{n=1}^{\infty}\left\{(M+1)\,\tau_0\left[A_n((M+1)\tau_0) - A_n(M\tau_0)\right] - n\left[A_{n+1}((M+1)\,\tau_0) - A_{n+1}(M\,\tau_0)\right]\right\} \cdot \left[\tan^{-1}\left[\frac{x}{2nH+D}\right] - \tan^{-1}\left[\frac{x}{2nH-D}\right]\right]. \tag{38}$$

It can be shown from (25) and (26) that

$$\lim_{M\rightarrow\infty}\left\{A_n[(M+1)\,\tau_0] - A_n(M\,\tau_0)\right\} M\,\tau_0 = 0. \tag{39}$$

Thus

$$\lim_{M\rightarrow\infty}\frac{1}{T}\int_0^T v(x,0;t;M)\, dt = \pm\frac{v_f}{2}. \tag{40}$$

The average velocity over one earthquake cycle is the average slip rate of the respective sides of the fault. We shall obtain corresponding results in the viscoelastic shear zone model after considering the appropriate form of shear zone loading.

3.2. Shear Zone Loading

Suppose that the shear zone contains a fault network $\{(x_0,D,v)_f\}$ accommodating a net relative velocity v_0:

$$\sum_f v_f = v_0. \tag{41}$$

The preceding results suggest two possible end-member methods of simulating loading of the shear zone depending on our notions of the flow pattern in the plastosphere. In both cases, it is assumed that each fault at $(x_0)_f$ undergoes steady slip at rate v_f between depths D_f and H;, that is, a portion of the lower schizosphere accommodates steady slip to varying degrees depending on the values of D_f for each fault.

In the first case, steady slip at rate v_f continues in the downward extension of each respective fault; i.e., flow in the plastosphere is constrained to be discontinuous at discrete boundaries $(x_0)_f$. It is convenient here to specify the arguments x_0 and D explicitly in (29): $u^{(2)}_{SZ}(x,0;t;x_0,D)$. We suppose that steady deep slip occurs in response to loading of the shear zone at $x = \pm L$ at the summed rate of all of the slipping segments, leading to the shear zone loading contribution

$$u_{\text{load}}(x,0;t) = \sum_f \left\{ u^{(2)}_{SZ}[(x,0;t;(x_0)_f,D_f] + \frac{v_f}{2}\frac{x}{L}t \right\}. \tag{42}$$

In the second case, steady slip beneath depth D_f terminates at depth H, and flow in the plastosphere is continuous. Shear zone loading in this case results solely from background block motions. The loading component is then the sum of steady slip from depth D_f to H beneath the various fault segments plus an imposed shear zone velocity field:

$$u_{\text{load}}(x,0;t) = \sum_f \left[u^{(2)}_{SZ}((x,0;t;(x_0)_f,D_f) - u^{(2)}_{SZ}((x,0;t;(x_0)_f,H) \right] + \frac{v_0}{2}\frac{x}{L}t. \tag{43}$$

3.3. Asymptotic Behavior of Viscoelastic Shear Zone Model

In the viscoelastic shear zone model, steady slip below depth H again leads to vanishingly small velocity as $t \to \infty$. Setting $D = H$ and taking the limit $\tau \to \infty$ in (29), we find that the velocity after the first n summations is

$$\lim_{t\to\infty} \partial_t u^{(2)}_{SZ}(x,0;t) = \frac{v_f}{\pi} G[x;x_0,L,2(n+1)H]. \tag{44}$$

Using the fact that $\lim_{h\to\infty} \coth \pi h/4L = \lim_{h\to\infty} \tanh \pi h/4L = 1$ and (A6), we obtain

$$\lim_{h\to\infty} G(x;x_0,L,h) = 0. \tag{45}$$

and thus taking $n \to \infty$ in (44),

$$\lim_{t\to\infty} \partial_t u^{(2)}_{SZ}(x,0;t) = 0. \tag{46}$$

As a corallary, for finite t the displacement field has the property

$$\partial_t u^{(2)}_{SZ}(\pm L,0,t) = 0, \tag{47}$$

which follows immediately from (31).

Equations (46) and (47) show that the asymptotic contribution of steady creep below depth D_f (equation (42)), to the velocity field at Earth's surface behaves as

$$\lim_{t\to\infty} \partial_t u_{\text{load}}(x,0;t) = \sum_f \frac{v_f}{2}\frac{x}{L} = \frac{v_0}{2}\frac{x}{L}$$
$$\partial_t u_{\text{load}}(\pm L,0,t) = \sum_f \frac{v_f}{2} = \frac{v_0}{2}. \tag{48}$$

Similarly, (46) and (47) show that the asymptotic contribution of steady creep restricted to the depth range $D_f < y < H$ again obeys (48). The surface velocity field produced sufficiently long after initiation of the system in the viscoelastic shear zone model is thus identical for both models of shear-zone loading.

The velocity in the viscoelastic shear zone model averaged over one earthquake cycle is $\pm\frac{1}{2}$ the slip rate of the considered fault. To prove this, we consider velocity at time t after the Mth elementary earthquake cycle in the viscoelastic shear zone model. This consists of a superposition of deformation from periodic earthquakes plus loading given by either (42) or (43):

$$v_{SZ}(x,0;t;M) = \left\{ \sum_{m=0}^{M} \partial_t u^{(1)}_{SZ}[x,0;t+(m-1)T] \right\} + \partial_t u_{\text{load}}(x,0;t+MT). \tag{49}$$

In the case that u_{load} is given by (42), i.e., steady creep in the entire region beneath the locked portion of the fault(s), we obtain for the average velocity during the $(M+1)$th cycle (including the earthquake which terminates the cycle):

$$\frac{1}{T}\int_0^T v_{SZ}(x,0;t;M)\,dt = \pm\frac{v_f}{2} + \frac{v_f}{\pi}\sum_{n=1}^{\infty}\left\{ (M+1)\,\tau_0\left[A_n((M+1)\tau_0) - A_n(M\tau_0)\right] - n\left[A_{n+1}((M+1)\,\tau_0) - A_{n+1}(M\,\tau_0)\right]\right\} \cdot \left[G(x;x_0,L,2nH+D_f) - G(x;x_0,L,2nH-D_f)\right]. \tag{50}$$

Use of (39) leads to

$$\lim_{M\to\infty} \frac{1}{T}\int_0^T v_{SZ}(x,0;t;M)\,dt = \pm\frac{v_f}{2}. \tag{51}$$

In the case that u_{load} is given by (43), i.e., steady creep restricted to $D_f < y < H$ for fault f, we obtain for the average velocity during the $(M+1)$th cycle the right-hand side of (50) plus

$$\frac{1}{T}\left[u^{(2)}_{SZ}(x,0;MT;(x_0)_f;H) - u^{(2)}_{SZ}(x,0;(M+1)T;(x_0)_f;H) \right].$$

Equations (46) and (39) then establish (51).

3.4. Evolution of Shear-Zone Deformation

I consider the deformation within a shear zone driven by steady slip of its sides (and possibly the deeper extensions of the rupturing fault planes) and periodic occurrence of characteristic earthquakes. I will examine the temporal evolution of the system to illustrate how the system approaches periodic behavior after sufficient time and to discern differences with the conventional viscoelastic coupling model.

In the following examples, a single fault at $x_0 = 0$ extending to depth D is embedded in an elastic plate of thickness H and a shear zone of half-width L. In one elementary earthquake cycle, steady slip occurs below depth D at rate v_f for a time interval of length T, after which a slip event of magnitude $\Delta u = v_f T$ occurs on the fault. Velocity in the laterally homogeneous model (LHM) (conventional viscoelastic coupling

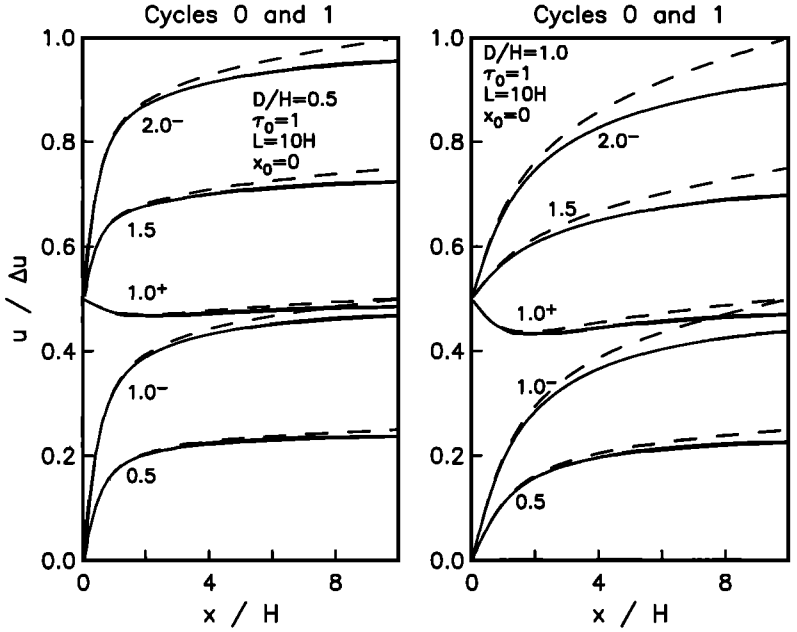

Figure 2. Cumulative fault-parallel displacement for the first two consecutive earthquake cycles of length T, each consisting of steady slip at rate v_f on the plane $x = x_0$ below depth D plus an earthquake above depth D with slip $\Delta u = v_f T$ terminating the cycle. Solid curves indicate laterally homogeneous model (equation (35)). Dashed curves indicate shear zone model (equations (42) and (49)) with $L = 10H$. The length of the earthquake cycle in units of plastosphere relaxation time is specified by τ_0. Numerals next to curves indicate elapsed dimensionless time in units of τ_0. The discontinuity in displacement upon entering a new cycle (i.e., $\tau = 1.0^-\tau_0$ versus $\tau = 1.0^+\tau_0$) is the coseismic effect of the earthquake at the end of the cycle (cycle 0 has only the effects of steady loading).

model) and the viscoelastic shear zone model (SZM) are calculated according to (35) and (49)/(42), respectively, for the initial cycles ($M = 0$ or 1) or later cycles ($M = 20$ or 21). Corresponding cumulative displacement from initial time $t = 0$ up to a specified time within these cycles is calculated straightforwardly as the time integral of (35) or (49). Both partial locking (D/H=0.5) and complete locking (D/H=1.0) will be considered.

Figure 2 shows cumulative displacement during cycles $M = 0$ and $M = 1$ for relatively large plastosphere viscosity ($\tau_0 = 1$ or, equivalently, $\eta = \mu T / 2$). Time is represented with dimensionless τ in multiples of τ_0. Displacement during cycle 0 reflects only the initiation of fault loading before any earthquake has occurred. The difference between the $\tau = 1.0^+\tau_0$ and $\tau = 1.0^-\tau_0$ curves is simply the coseismic offset of the first earthquake. Slight differences between displacements on the

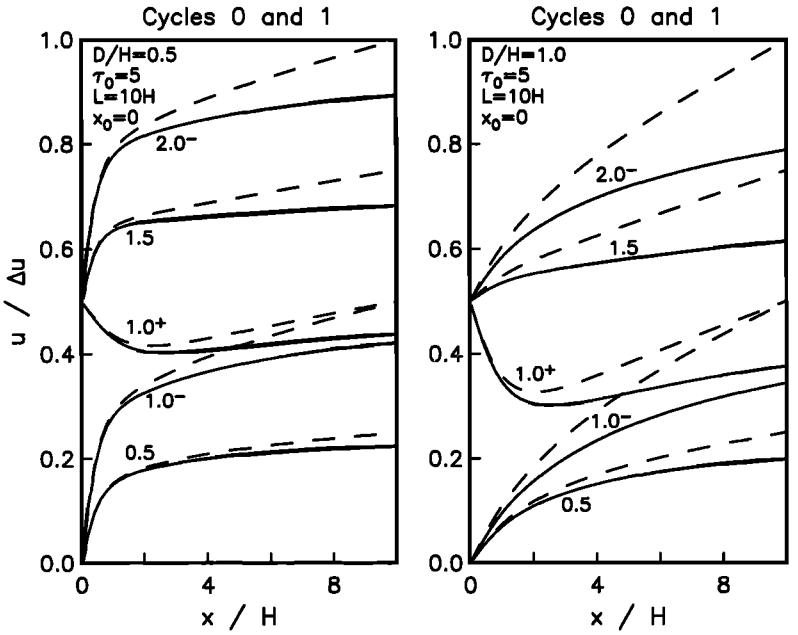

Figure 3. Same as Figure 2, but with $\tau_0 = 5$.

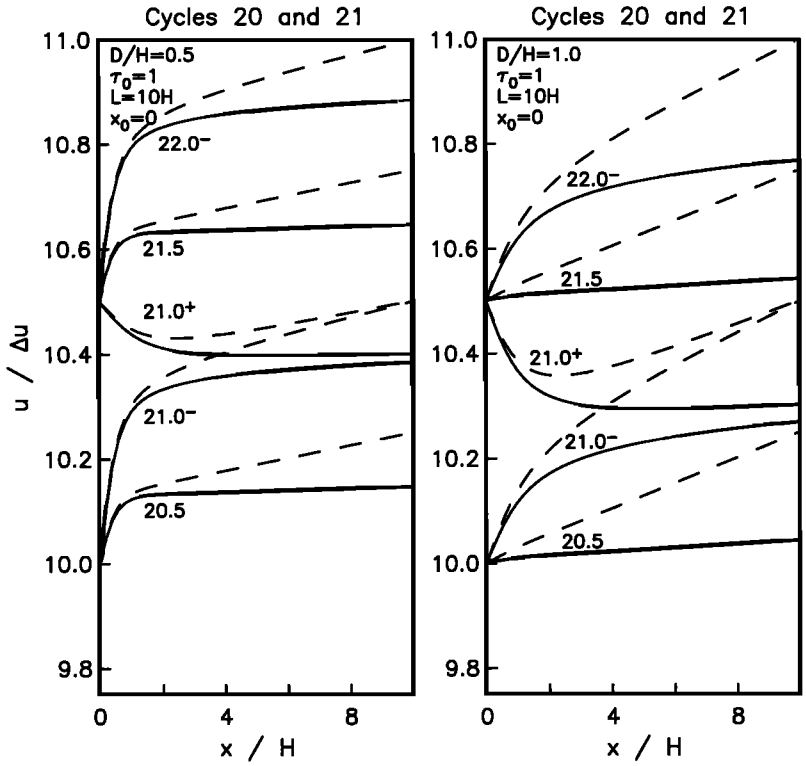

Figure 4. Same as Figure 2, but for cycles 20 and 21.

LHM (solid curves) and SZM (dashed curves) reflect the fact that the shear zone walls ($x = \pm 10H$) move at constant velocity $\pm v_f/2$ in the shear zone model but less than the steady slip rate below depth D (also $v_f/2$) on the laterally homogeneous model because of the retarding effect of the locked fault interface. Deformation during cycle 1 ($\tau \geq 1.0^+\tau_0$) is generally characterized by a greater relative velocity of the boundary $x = \pm 10H$ on the laterally homogeneous model because of the additional contribution of postseismic relaxation following the first earthquake. Differences between the LHM and SZM are

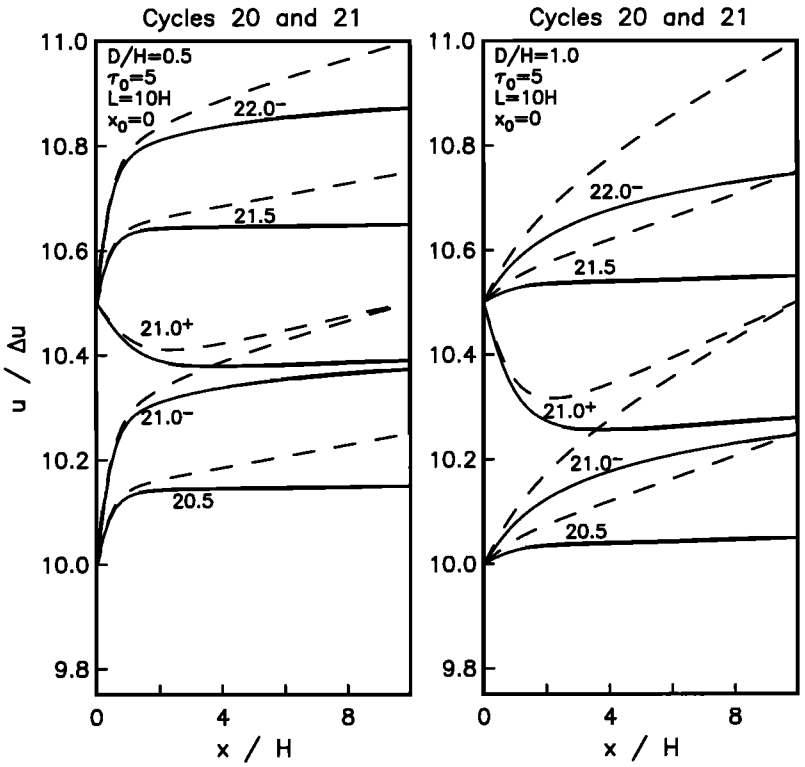

Figure 5. Same as Figure 2, but with $\tau_0 = 5$ and for cycles 20 and 21.

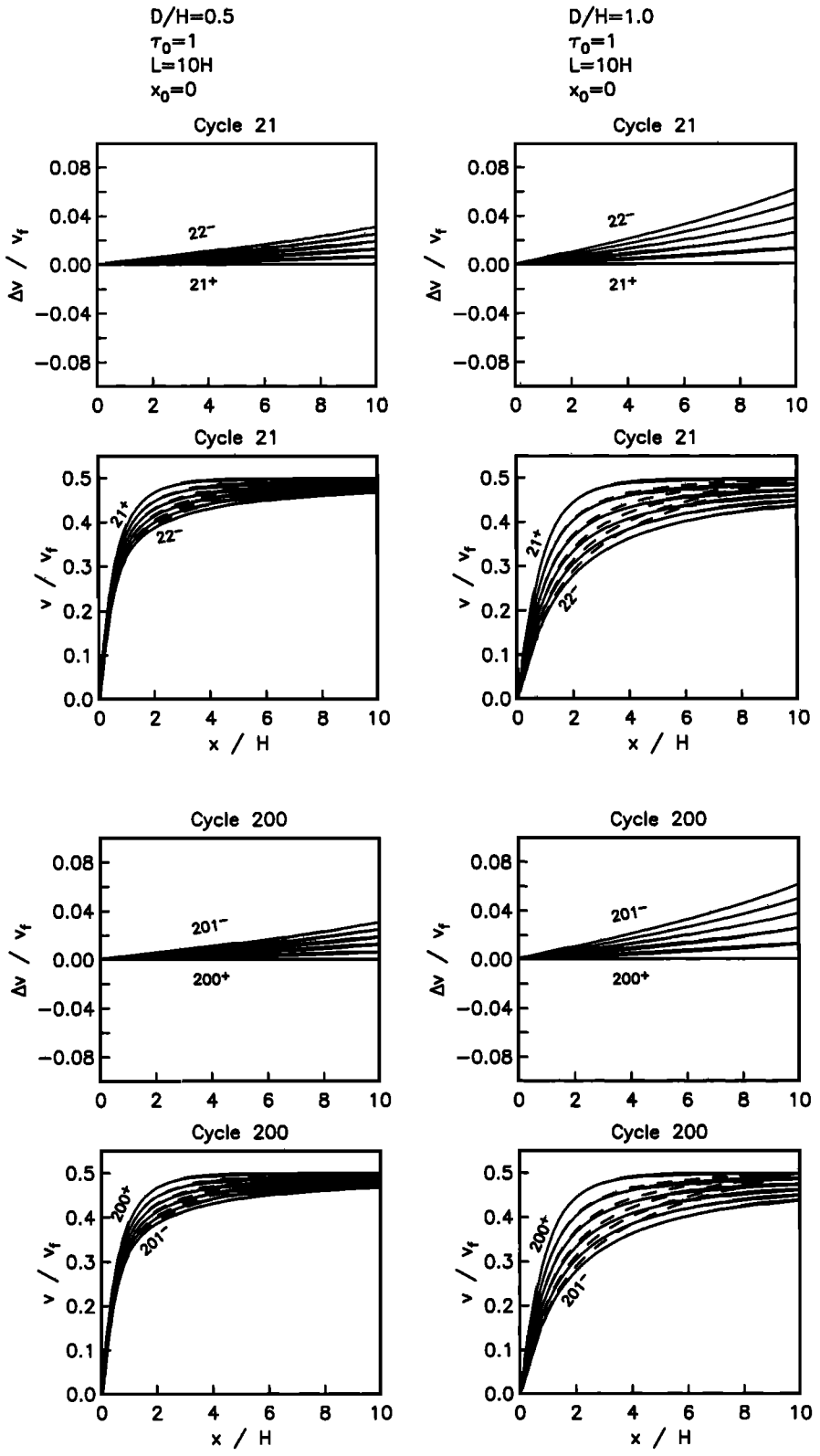

Figure 6. Fault-parallel velocity at specified times during cycles 21 and 200 with indicated model parameters. Solid curves indicate laterally homogeneous model (equation (35)). Dashed curves indicate shear-zone model (equations (42) and (49)) with $L = 10H$. Each top panel displays the difference between the shear zone model velocity and laterally homogeneous model velocity. Numerals next to curves indicate elapsed dimensionless time in units of τ_0. A total of six curves span a given cycle in increments of 0.2 τ_0 (i.e., $\tau = 21.0^+ \tau_0$, $\tau = 21.2\ \tau_0$, $\tau = 21.4\ \tau_0$, $\tau = 21.6\ \tau_0$, $\tau = 21.8\ \tau_0$, and $\tau = 22.0^- \tau_0$ for cycle 21).

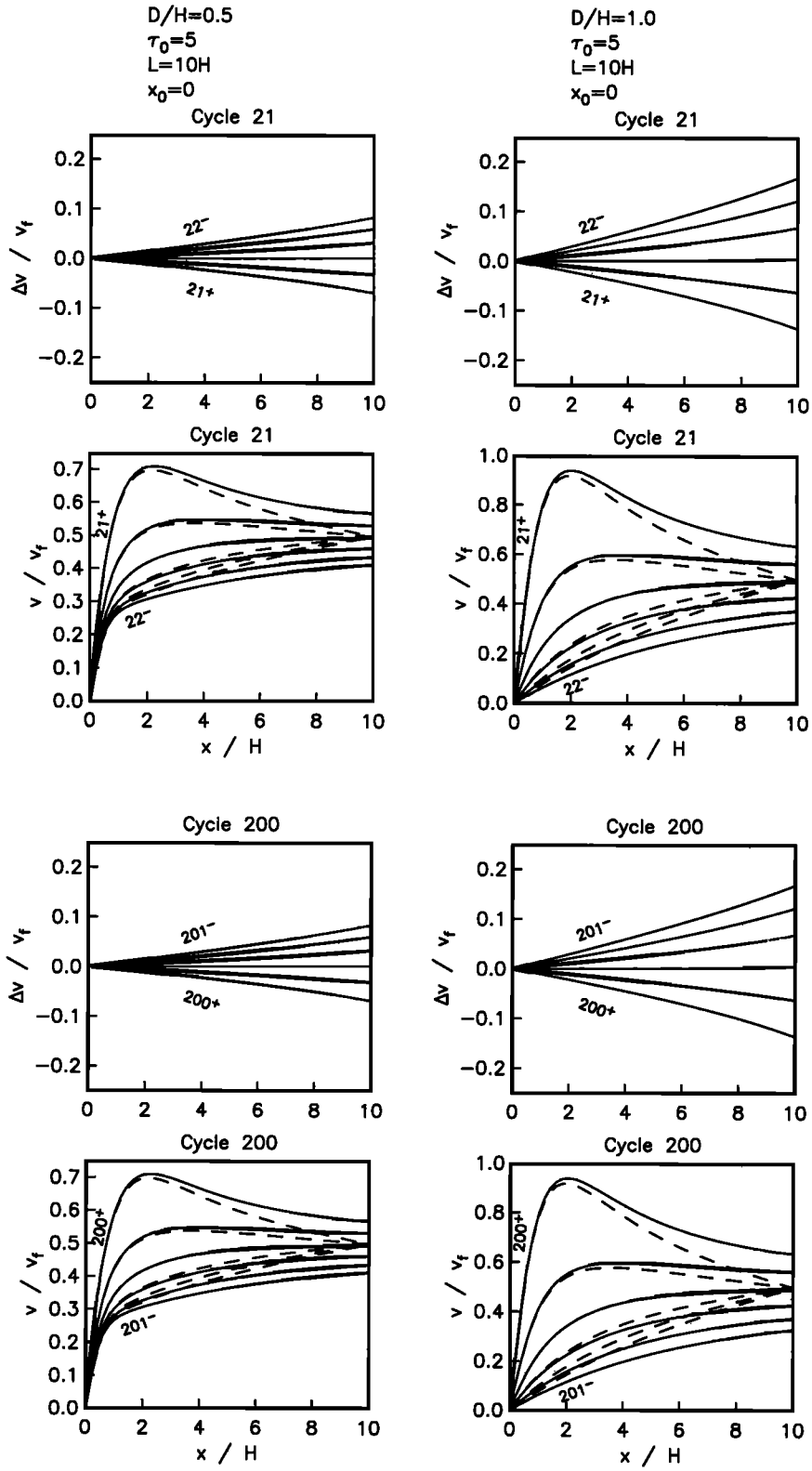

Figure 7. Same as Figure 6, but with $\tau_0 = 5$.

more pronounced when D/H is increased and when τ_0 is increased (Figures 2 and 3). Loading effects from steady slip beneath the fault are, as expected, diminished both for higher D/H and higher τ_0. In the latter case, viscosity is relatively low and the transfer of loading stress from the plastopshere to the schizosphere is consequently dampened.

The displacement patterns during cycles 20 and 21 shown in Figure 4 ($\tau_0 = 1$) and Figure 5 ($\tau_0 = 5$) follow the same patterns, but at this more evolved stage the differences between the LHM and SZM apparently depend mostly on D/H rather than on τ_0. This reflects the insensitivity of both models to loading below depth H after sufficient time has passed, so that the differences between the LHM and SZM are to a large extent inherited from the initial retardation of the LHM This is espe-

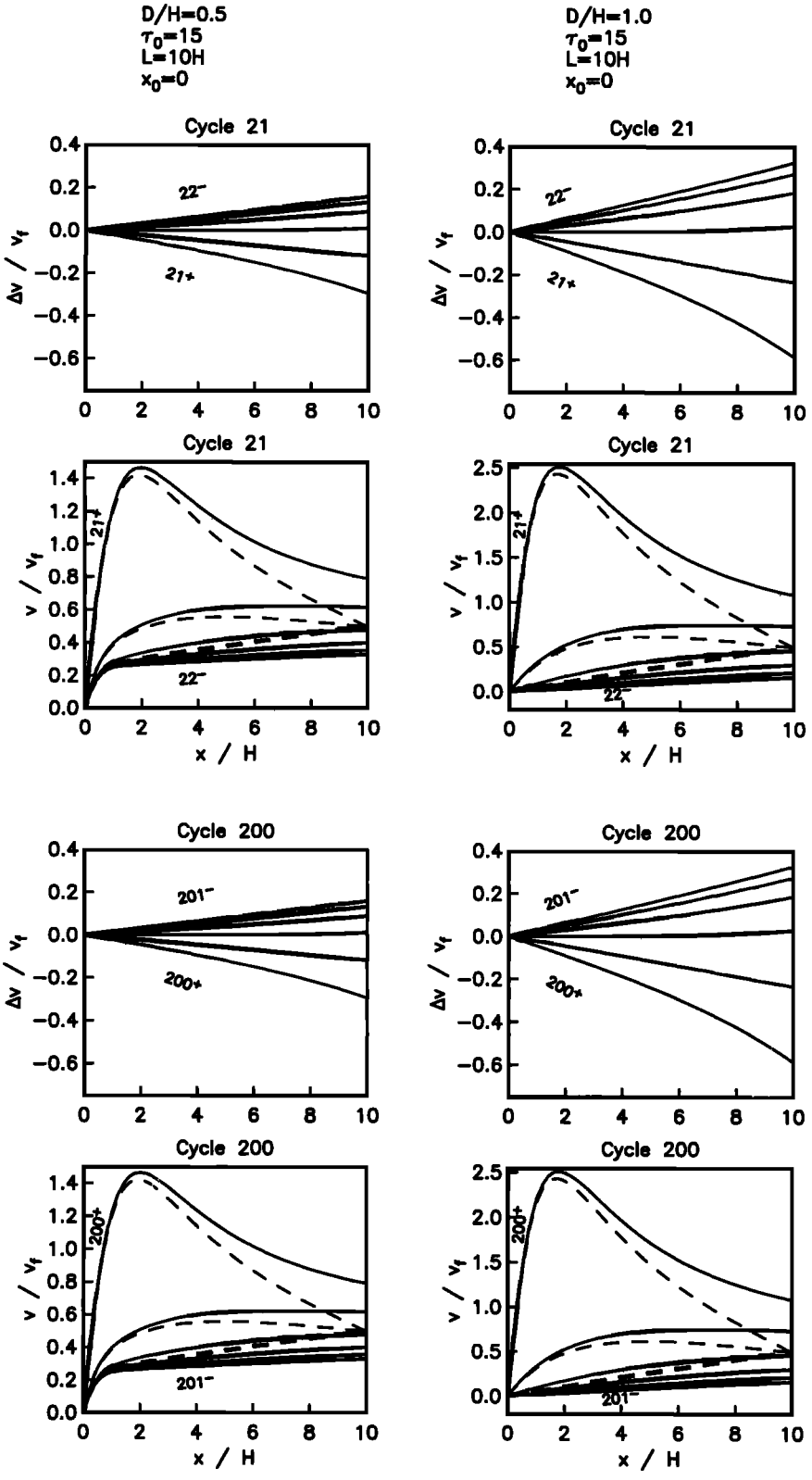

Figure 8. Same as Figure 6, but with $\tau_0 = 15$.

cially apparent for the case $D / H = 1.0$ and $\tau_0 = 5$, where the large differences existing at the end of cycle 1 ($\tau = 2.0^-\tau_0$ in Figure 3) are maintained even after the system is highly evolved ($\tau = 22.0^-\tau_0$ in Figure 5). These differences are not related to the neglect of coseismic offsets at the shear zone edges in the SZM since most of the initial retardation of the LHM occurs during cycle 0 and prior to the first earthquake. Even a conservative comparison of time N^- displacement on the SZM with time N^+ displacement on the LHM shows strong retardation of the LHM at all integral cycle times N.

The displacement patterns sampled in increments of one-half cycle in Figures 2-5 conceal, however, large variations in velo-

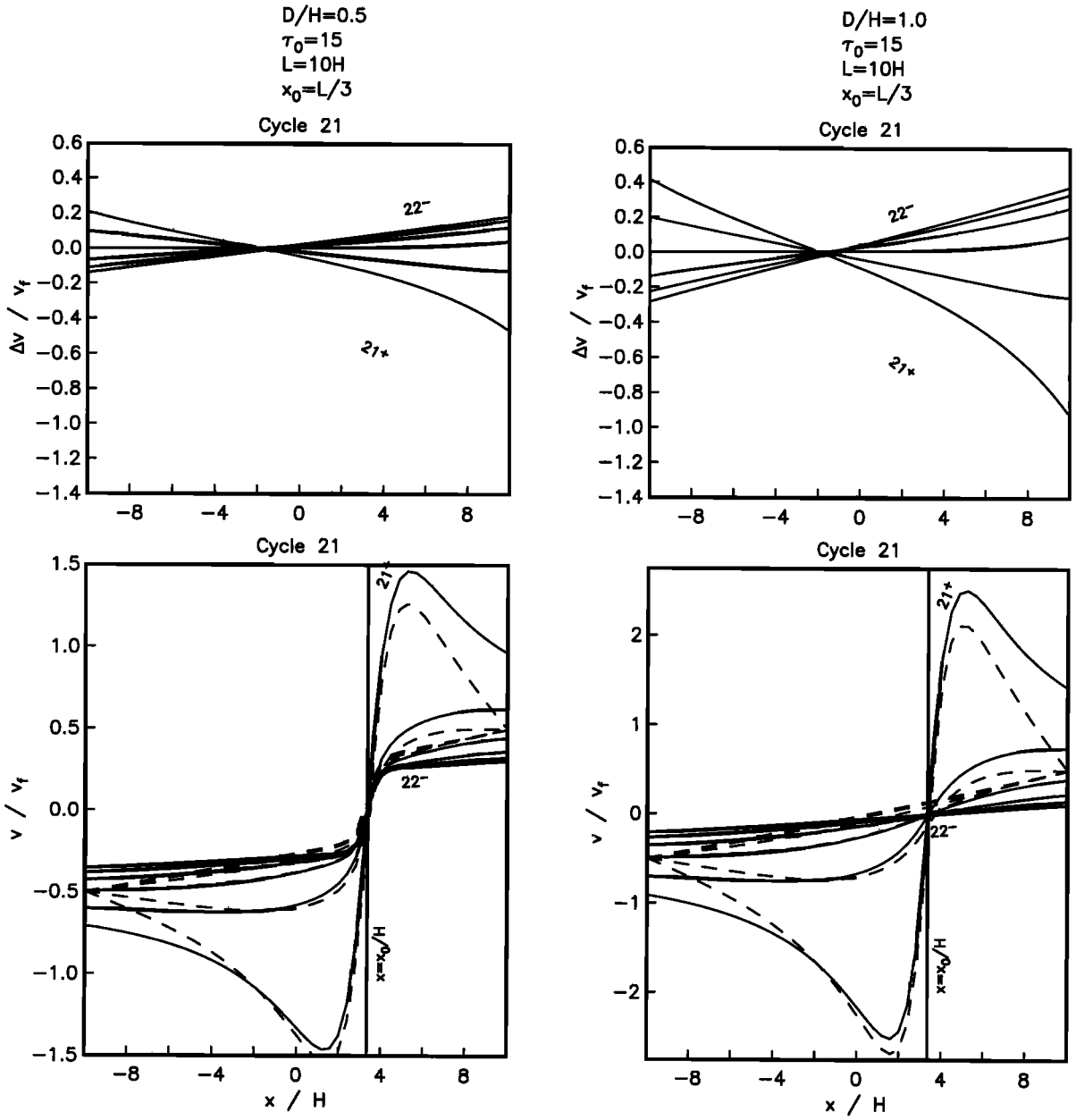

Figure 9. Same as Figure 6, but with $x_0 = L/3$ and $\tau_0 = 15$ (cycle 21 only).

city within a cycle and corresponding differences between the spatial and temporal velocity patterns of the two models. Figures 6 and 7 show the velocity patterns in cycles 21 and 200 for the same groups of model parameters considered previously ($\tau_0 = 1$ or 5, respectively). Figure 8 shows the velocity pattern for $\tau_0 = 15$. Figures 6, 7, and 8 together thus track the model responses through $\tau_0 = 1$, 5, and 15. Figures 6-8 reveal small (up to 6% of v_f) differences between the LHM and SZM for $\tau_0 = 1$, modest differences (up to 17%) for $\tau_0 = 5$, and large differences (up to > 50%) for $\tau_0 = 15$. Larger D/H generally produces greater differences between the two models. In all cases, differences in velocity patterns between cycles 21 and 200 are <0.5%, so all systems considered are essentially evolved to maturity by the time of the 21st cycle.

In the preceding cases the fault is centered on the shear zone ($x_0 = 0$), and thus all deformation is symmetric. In Figure 9 we consider the case $x_0 = L/3$ in which the distances of the fault from the shear zone edges are in the ratio 2:1, other parameters being chosen as in Figure 8 (low-η plastosphere). This deformation remains symmetric for the LHM (i.e., zero velocity at $x = x_0$) but is generally nonsymmetric for the SZM. The velocity differences between the LHM and SZM are greater than for the equivalent nonsymmetric deformation, reaching > 300% near the "short" shear zone edge ($L/3 < x < L$). Interestingly, the absolute velocities of the fault zone itself for the two models generally differ, and a narrow region where velocity differences between the two models are minimized ($\Delta v \sim 0$) is located on the other side of the shear zone near $x \sim -L/10$.

3.5. Accuracy of SZM Formulation

In the preceding comparisons, it is important to consider the accuracy of the image solution used to derive the SZM, in which coseismic offsets of the shear zone edges $x = \pm L$ have

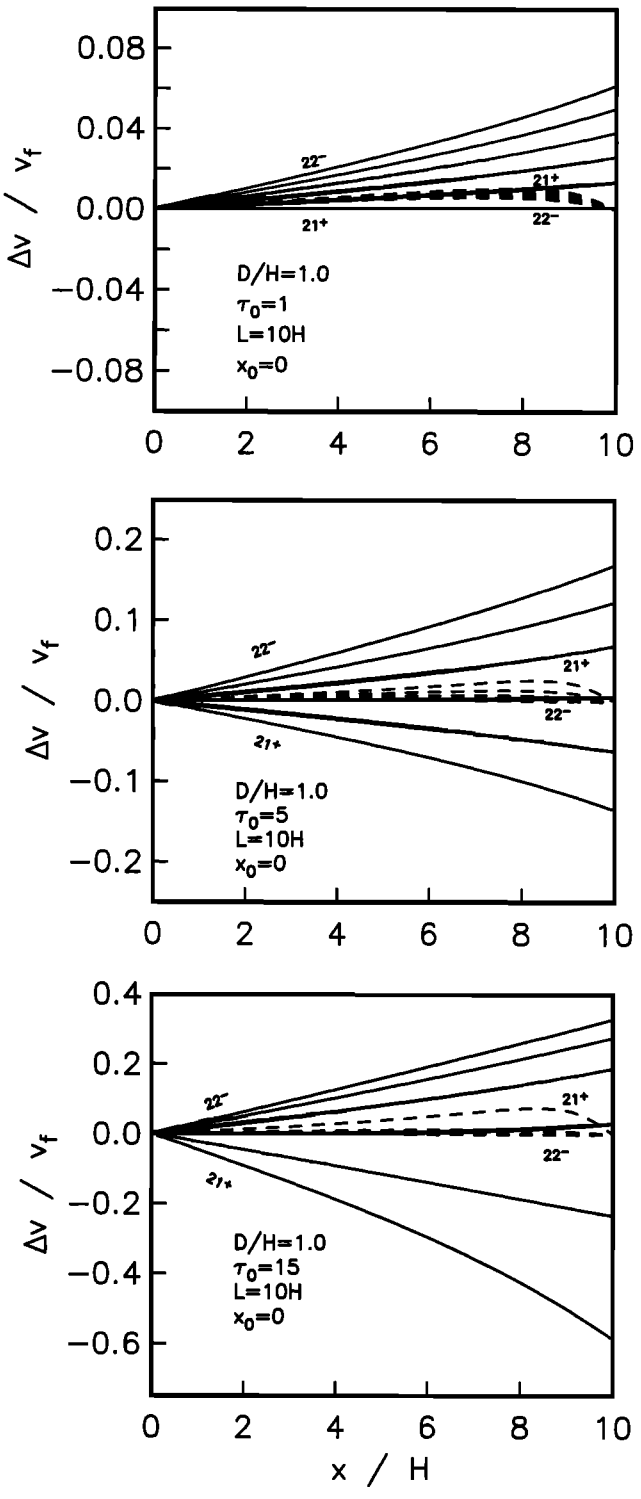

Figure 10. Bias in the velocity field during cycle 21. Dashed lines indicate upper bound velocity response of the SZM to time-periodic edge perturbations specified by the episodic coseismic slip at the shear zone edges, evaluated during cycle 21. Solid lines indicate corresponding difference between SZM and LHM velocity field for previously considered cases with $D/H=1$.

been assumed negligible. This approximation could be removed exactly by introducing small distributed sources at the shear zone edges acting episodically with the fault motions but also continuously fluctuating slightly throughout the seismic cycle such that the average perturbation on the edges over one cycle (including the coseismic offset) is zero. The temporally continuous fluctuation is of the same order of magnitude and tends to nullify the episodic perturbation. Thus I consider specifically the episodic perturbation, which can be calculated exactly by means of a simple image solution of periodicity $4L$ and depth-dependent slip equal to the coseismic slip of the original system evaluated at $x=\pm L$. This is just a sum of two SZM solutions with dislocation sources at $x=\pm L$.

In all models considered here, the depth-dependent edge perturbation in question does not exceed 1.6% (of Δu) for $D/H=0.5$ or 3.2% for $D/H=1.0$. To place an upper bound on the possible time-dependent velocity response of the system to a time-periodic perturbation of this type, it may first be noted that this response depends on the depth dependence of the edge perturbations. If the edge perturbations were uniform and extending to infinite depth, the system would respond instantaneously by producing a simple shear across the shear zone with identically zero subsequent velocity perturbation. Thus a significant velocity perturbation produced by uniform edge perturbations at $x=\pm L$ from depth 0 to H is balanced by an equal but opposite velocity perturbation produced by uniform edge perturbations from depth H to ∞. It follows that a conservative estimate of the velocity response of the system to the actual edge perturbations is obtained by specifying uniform edge perturbations from depth 0 to H with the above magnitudes. The resulting bias in the velocity field during cycle 21 is shown in Figure 10 together with the corresponding velocity differences between the SZM and LHM for the previously considered cases with $D/H=1$. The velocity bias is likely smaller than these estimates because given $|x_0 \mp L| \gg H$, the $x=\pm L$ edge perturbations considered should be nearly uniform from the surface to a depth significantly greater than H. I interpret the much larger differences between the LHM and SZM as almost entirely due to the very different relaxation behavior exhibited by them, which is due fundamentally to the fact that the two quarter-space volumes of plastosphere which bound the shear zone may relax in the LHM but remain rigid in the SZM.

4. Implications for Mechanics of Strain Accumulation in Southern California

4.1. Properties of Velocity Variation During a Cycle

An ubiquitous property of the low-viscosity (high τ_0) simulations is that the LHM velocity greatly exceeds the SZM velocity early in a mature cycle, but the roles are reversed later in the cycle with the SZM velocity greatly exceeding the LHM velocity. Although both models possess large velocity variations within a cycle, it is clear from Figures 7 and 8 that the LHM exhibits the largest velocity variations. In the $\tau_0 = 15$ case, LHM velocity exceed $v_0/2$ by 150% ($D/H = 0.5$) or 400% ($D/H = 1.0$) during the first third of the cycle but decreases to 67% ($D/H = 0.5$) or 34% ($D/H = 1.0$) of $v_0/2$ during the final third of the cycle. The SZM exhibits more moderate variations during the cycle. The results for $\tau_0 = 5$ (Figure 7) and $\tau_0 = 15$ (Figure 8) show that its velocity pattern approaches that of a simple shear zone during the second half of the cycle.

There are significant differences in the spatial and temporal patterns between laterally homogeneous deformation produced by a fault loading and rupturing cycle and the corresponding deformation produced within a finite width shear zone. Whether one model or the other applies depends on the viscoe-

Table 1. 2D Shear Zone Parameters of San Andreas Fault, Mojave Segment

Fault System	L, km	H, km	D/H	x_0, km	v_f^a, mm/yr	T, years	t, years
San Andreas	300	12–18	0.5–1	0	34	200–330	124–169
Eastern California Shear Zone	300	12–18	1	125	9	10^4	10^4

[a] Right-lateral slip rate parallel to the Mojave segment

lastic structure around the fault zone. One criterion for defining the edge of a shear zone may be where gradients in geodetically measured velocity decrease to very small level, as *Dixon et al.* [2000] have suggested for delineating the western boundary of the Eastern California Shear Zone north of the Garlock fault. This notion would require that the geodetic observations in question be observed relatively late in a cycle, as early postseismic transients can produce zero or even negative shear strains near the fault. An alternative criterion is that regions of relatively thick lithosphere which bound a strike-slip fault zone must possess a cooler geotherm than the fault zone itself, and if viscosity is primarily thermally controlled, then the bounding thick lithospheric blocks (belonging to presumably different tectonic plates) will behave macroscopically as elastic boundaries and can be well approximated as rigid boundaries. Without considering the origin of thermal differences between the fault zone and surrounding thicker lithosphere, the above two criteria are related in the sense that the fault zone will behave mechanically as a thin stress guide and the bounding blocks will behave as a thick stress guide which is relatively difficult to deform [e.g., *Kusznir*, 1991].

4.2. Mojave Segment of the SAF

4.2.1 Delineation of Shear Zone. The above criteria may be applicable to the southern SAF system. I choose to focus on the Mojave section of the SAF because available data are of high quality and the fault systems which contribute to long-term deformation are fairly well understood. These are the SAF system and the Eastern California Shear Zone (ECSZ). The southwest boundary of a shear zone bounding these fault systems may be defined by the contact of continental lithosphere with oceanic lithosphere ~300 km southwest of the SAF [*Trehu*, 1991]. Beginning ~80 km northeast of the Mojave segment, the ECSZ defines a ~200-km-wide zone of active faulting [*Unruh et al.*, 1994] which includes the faults which ruptured in the 1992 Landers and 1999 Hector Mine earthquakes. The large width of the deformation zone based on faulting patterns is consistent with the fault-parallel velocity pattern around the Mojave section of the SAF [*Shen et al.*, 1996], which suggests that the actively shearing zone extends from at least -200 km southwest to +150 km northeast of the SAF. I interpret the faulting pattern as roughly defining a shear zone of half width L ~ 300 km, inclusive of the breadth of deformation spanned by the offshore Santa Lucia Escarpment [*Trehu*, 1991] to the southern Death Valley fault zone at the eastern end of the ECSZ. Other parameters defining the SAF system and ECSZ are summarized in Table 1. The San Andreas fault is placed in the middle of the shear zone (x_0=0) on the basis of the symmetry of the observed fault-parallel velocity field with respect to the San Andreas fault [*Shen et al.*, 1996]. The seismogenic layer depth D in the 12–18 km range is considered appropriate for the region [*Webb and Kanamori*, 1985; *Jones*, 1988; *Hill et al.*, 1990]. For concreteness and because of the ~15 km depth extent of faulting during the 1992 Landers earthquake [*Wald and Heaton*, 1994], the ECSZ fault system is assumed locked along the entire elastic layer, i.e., $D = H$. I consider a range of locking depths for the SAF system ranging from $0.5 \le D/H \le 1.0$. The mean slip rates v_f accommodated across these faults and their corresponding repeat times T are consistent with estimates from the literature [e.g., *Savage et al.*, 1990; *Feigl et al.*, 1993; *Sauber et al.*, 1994; *Shen et al.*, 1996; *Rubin and Sieh*, 1997]. The chosen values of 34 and 9 mm/yr for the long-term fault-parallel slip rate of the SAF and ECSZ, respectively, predict 43 mm/yr parallel to the Mojave segment of the SAF (which strikes N65°W) and 50 mm/yr being accommodated within the 600-km-wide shear zone parallel to the local Pacific-North America motion direction (which strikes N35°W). This is consistent with the 51 mm/yr Pacific-North America relative plate velocity estimated by *DeMets and Dixon* [1999] and the Vandenberg-North America velocity of 48.4 mm/yr determined by VLBI measurements [*Gordon et al.*, 1993].

4.2.2 Characterization of earthquake cycle. For observations recorded from 1971 to 1992, *Savage and Lisowski* [1998] argued that a time $\tau/\tau_0 \sim 0.6 - 0.8$ into the present cycle likely applies to southern California, on the basis of an assumed average repeat time T of large events of 150 to 200 years and the time since the last large event (1857). Clustering of large events, however, is documented such that two large events closely spaced in time tend to rupture the entire 600 km long span of the SAF from the Parkfield to Indio segments, with cluster repeat times of 200 to 330 years [*Sieh et al.*, 1989]. The characterization of the earthquake cycle in this region in terms of such clusters better satisfies the 2-D assumption of the modeling and has less scatter than the repeat times of individual large historic events. Given the 136 to 157 years elaspsed since the mean time of the last cluster (1812 and 1857 events), recent observations would correspond to a time $\tau/\tau_0 \sim 0.4 - 0.8$. If the observations are dominated by relaxation effects following the two most recent clusters, then the upper end repeat time of 330 years applies, and recent observations would correspond to a time $\tau/\tau_0 \sim 0.4$–0.5 into the present cycle. In contrast, the large repeat time T for the ECSZ does not need to be accurately known since the observation time to be considered is only a few years before the 1992 Landers, 1999 Hector Mine sequence in the ECSZ, i.e., t/T is very close to 1 for the ECSZ. For any reasonable viscosity value which applies to the region (10^{18} Pa s $<\eta<10^{20}$ Pa s), τ is very large for the ECSZ, and the LHM and SZM solutions reduce to their asymptotic behavior, i.e., simple shear at the appropriate rate (9 mm/yr) for the SZM and zero for the LHM. Thus the differences to be encountered between the LHM and SZM partially reflect the sampling of the velocity field about four tenths of the way through the present SAF earthquake cycle but more tangibly reflect the sampling of it near the end of a very long earthquake cycle in the ECSZ.

4.2.3 Modeling of Fault-Parallel Velocity Field *Savage and Lisowski* [1998] have noted that the strain field as observed by trilateration networks close to the big bend section of the SAF is well-described in terms of steady slip below an apparent locking depth of 30 km [*Savage and Burford*, 1973], much deeper than could be plausible with a brittle-ductile transition of ~15 km. The fault-parallel velocity around the entire Mojave section of the SAF [*Shen et al.*, 1996] out to ~200 km from the fault is also unusually broad. The velocity field determined by *Shen et al.* [1996] is based primarily on trilateration and GPS data covering the time interval 1971 to 1993 and is essentially a picture of the interseismic velocity field free from 1992 Landers or 1994 Northridge earthquake perturbations. (Where necessary, Shen et al. performed a correction for the coseismic offsets of the Landers earthquake.)

Given the ~600 km length of repeating southern SAF earthquakes compared with the aperture of the observations, a 2-D geometry is assumed applicable. Figure 11 compares observed fault-parallel velocity with the predictions of the LHM and SZM for various choices of dimensionless SAF cycle time τ_0, assuming H=15 km (SAF and ECSZ) and D/H=0.9 (SAF). Other parameters are prescribed by Table 1. The curves shown in Figure 11 are labeled according to the value of τ/τ_0 for the SAF system during the 21st cycle. If the observations do indeed correspond roughly to a time ~ 0.4–0.5 τ_0 into the present SAF cycle, then the SZM is found to provide a better fit to the data. This is most clearly seen for the case τ_0 = 12 (which yields better fits to both the SZM and LHM than the other values of τ_0) and at observation distances > 100 km from the SAF, where observed velocities fall close to τ = 0.4 or 0.5τ_0 for the SZM but depart significantly from τ = 0.4 or 0.5τ_0 for the LHM.

A grid search over a wide model space confirms the better performance of the SZM. Misfit was calculated according to

$$\chi^2_r(H,D,\tau_0) = \frac{1}{N}\sum_{i=1}^{N}\left[\frac{v^i_{obs} - v^i_{cal}}{\sigma_i}\right]^2, \quad (52)$$

where χ^2_r is reduced χ^2, N=71 is the number of observations, v^i_{obs} is observed velocity at point i, and v^i_{cal} is calculated velocity at point i for the given H, D, and τ_0, assuming τ = 0.45τ_0. Figure 12 shows three slices of the misfit pattern obtained in $H - D/H - \tau_0$ space for both the LHM and SZM. The minimum misfit obtained in each slice is labeled with a cross. There is only marginal difference in the results for different values of H. Minimum misfit ranges are 2.86 (H=12 km), 3.01 (H=12 km), and 3.15 (H=18 km) for the LHM; 2.21 (H=12 km), 2.24 (H=15 km), and 2.25 (H=18 km) for the SZM. Optimal τ_0 tends toward slightly lower values as H is increased, and the LHM produces generally lower values of optimal τ_0 than the SZM. If the SZM applies and H=15 is the appropriate elastic layer thickness, then a range of τ_0 = 9–13 and D = 12–15 km is obtained (Figure 12).

4.3. Applicability of SZM Versus LHM

Given the fits of the data with the three parameters H, D, and τ_0, the addition of the one parameter L, the shear zone width in the SZM, is highly significant. A simple F test shows that the improvement in minimum χ^2_r obtained by choosing L=300 km, in addition to the other three parameters, is found to be significant at the 99.98% confidence level. Although this strongly suggests that the SZM is a better description of the seismic cycle in southern California than the LHM, several unmodeled factors might affect this evaluation. The sharp contrast in seismic velocity across the Garlock fault [e.g., *Humphreys and Dueker*, 1994] suggests that the Sierra Nevada block is relatively cooler at uppermost mantle depths compared with the Mojave desert, suggesting a sharp contrast in plastosphere viscosity across the Garlock fault. Thus the assumption of uniformity of material properties parallel to the fault used in the 2-D modeling is only approximately satisfied. The modeling also assumes that the elastic shear modulus is vertically uniform, whereas mantle shear modulus is typically about twice as large as the crustal value. This has a potentially significant effect on the coseismic displacement field produced by strike-slip faulting [*Pollitz*, 1996], but postseismic behavior is governed primarily by the Maxwell relaxation time of the plastosphere, which can be kept constant by scaling plastosphere viscosity with the shear modulus.

Both the LHM and SZM are subject to these limitations. The LHM, however, suffers from the additional limitation that <~39 mm/yr relative velocity parallel to the Pacific-North America motion is predicted at τ ~ 0.4–0.5 τ_0 over a several hundred kilometer width centered on the SAF. This falls short of the 46 mm/yr relative velocity between VLBI sites Vandenberg and Flagstaff [*Gordon et al.*, 1993] located southwest and northeast of the SAF, respectively. The fact that the SZM satisfactorily matches both the VLBI and plate motion constraints on local Pacific - North America relative motion, whereas the LHM does not, is a direct consequence of the opacity of the LHM to strain accumulation on the ECSZ near the end of its cycle. It is difficult to see how the LHM could be rectified to account for the missing velocity.

In both models the 2-D assumption may be only marginally valid for the ECSZ. The combined 1992 Landers and 1999 Hector Mine ruptures account for at most a 100 km length of the ECSZ, and only this portion is known for certainty to have been late in a seismic cycle when recent measurements were made. This leaves open the possibility that signals from other ECSZ events preceding the earliest VLBI measurements ~1980, particularly north of the Landers rupture zone, could contribute to interseismic velocity in the LHM. Tangible signals from such earthquakes, however, would be contingent upon the observation period being relatively soon following the earthquake(s), within a few dedades if the viscoelastic stratification determined by *Pollitz et al.* [2000] for the Mojave desert region is applicable. Relaxation following the 1871 Owens Valley earthquake might contribute an observable signal north of the Garlock fault [*Dixon et al.*, 2000], but the predicted contribution to the Vandenberg-Flagstaff motion in 1980 is only 0.4 mm/yr, assuming that the 1871 earthquake was twice as large as the Landers earthquake. This does not account for the >~7 mm/yr of missing fault-parallel velocity in the LHM.

4.4. Plastosphere Viscosity

Both the LHM and SZM imply similar values of τ_0 ~ 10 for the dimensionless length of the seismic cycle (Figure 12). Assigning the value μ = 30 GPa to the rigidity then leads to an estimate of plastosphere viscosity $\eta = 1.6 \times 10^{19}$ Pa s. (The viscosity is proportionally higher if account is made for the larger rigidity for the mantle.) This value is ~2–3 times larger than the crust and mantle viscosity estimates of *Pollitz and Sacks* [1992] based on analysis of postseismic relaxation fol-

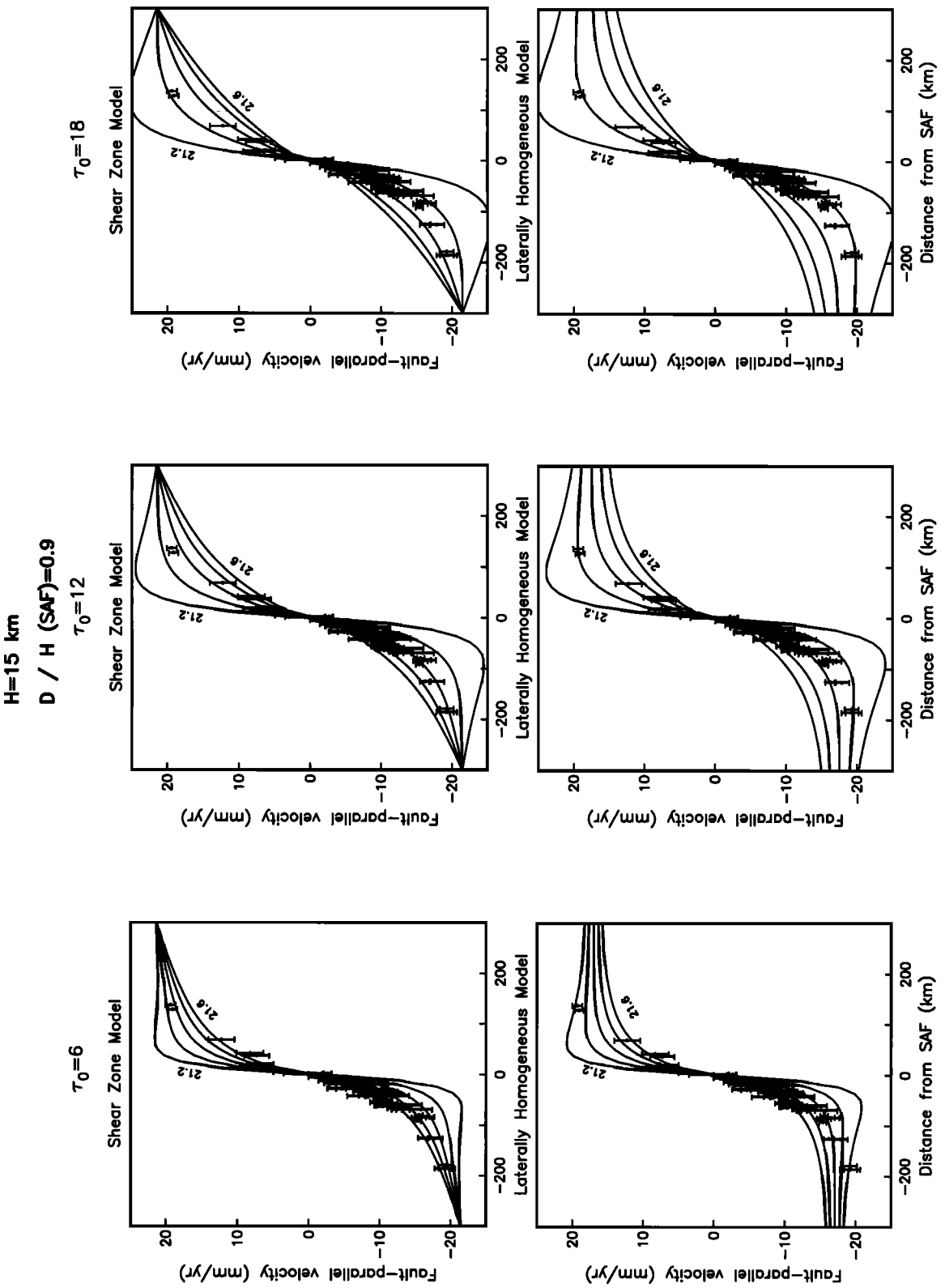

Figure 11. Deformation in the Mojave section of the SAF according to three different models with varying dimensionless SAF cycle time τ_0, taking fixed elastic layer thickness H and seismogenic layer thickness D. The value of H for the ECSZ is identical to the value assigned to the SAF. All other model parameters are prescribed by Table 1. Observed fault-parallel velocity [*Shen et al.*, 1996] is superimposed with ± 1 standard deviation on each side of the plotted point.

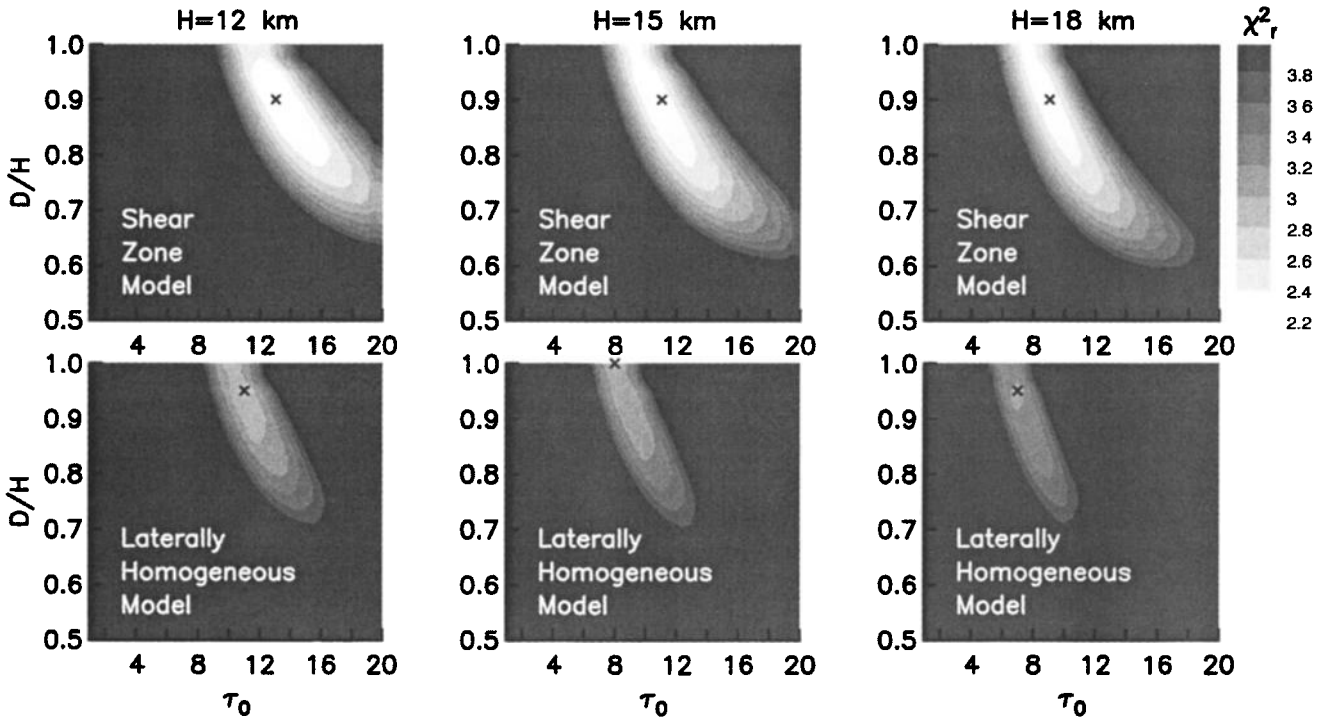

Figure 12. Fits of LHM and SZM to fault-parallel interseismic velocity data around the Mojave section of the SAF [*Shen et al.*, 1996]. Three slices of reduced χ^2 in $H - D/H - \tau_0$ space are calculated using equation (52) as a function of these three parameters, other parameters being prescribed by Table 1, assuming that the observations correspond to a time $\tau=0.45\tau_0$ into the present cycle.

lowing the 1857 Fort Tejon earthquake. A possible explanation fo the differing viscosity estimates may be lateral and vertical variation in viscosity. In addition, the plastosphere is probably not a Maxwell viscoelastic material but likely possesses a nonlinear stress-strain relation of the form $\dot{\varepsilon} = A\ \sigma^n$, where σ and $\dot{\varepsilon}$ are the second invariant of the stress and strain rate tensor, respectively, A is a constant which depends on temperature, pressure, and the material, and n is a constant ~3. *Pollitz et al.* [2000] hypothesize that such a stress-strain relation may explain the relatively large strain rates (~10 times the interseismic strain rate) observed for the immediate postseismic epoch following the M7.3 1992 Landers earthquake, compared with the more moderate strain rates (~3 times the interseismic strain rate) during the subsequent 3 years after σ had presumably relaxed somewhat. The stress change following the M8.3 1857 Fort Tejon earthquake were larger and perhaps more long-lived than that following the Landers earthquake. Relatively high σ following the Fort Tejon earthquake may have persisted for the 2 to 3 dedades spanning the triangulation observations used in the modeling of *Pollitz and Sacks* [1992]. This may have led to a tangible influence of the nonlinear effect and reduced the effective viscosity associated with these observations.

5. Conclusions

I have reexamined the behavior of a 2-D strike-slip fault zone in an elastic-viscoelastic coupled medium in order to investigate the effect of embedding the system in a finite width shear zone. For simplicity, focus has been on a system consisting of a schizosphere (elastic upper crust) overlying a uniform Maxwell viscoelastic plastosphere. The strike-slip fault occupies a portion of the schizosphere, and the considered models account for loading of the fault by constant motion of the shear zone edges and (possibly) steady slip on the deeper extension of the fault, periodic rupture of the fault, and postseismic relaxation.

The conventional (laterally homogeneous) viscoelastic coupling model is driven by dislocation sources only on the fault plane and its deeper vertical extension. It possesses the properties that after sufficient time after initiation of the system, (1) the average velocity during a complete elementary earthquake cycle is the average slip rate of the side of the fault of the considered point and (2) the far-field velocity approaches the same constant slip rate. In the viscoelastic shear zone model we impose the constraint that the velocities of prescribed shear zone edges be constant. The deformation in the shear zone system is obtained by transformation of the laterally homogeneous system by employing an infinite sequence of image sources parallel to the fault plane, and it is found to satisfy the same long-term average behavior (i.e., properties 1 and 2 above) as the conventional system. The assumed constant velocity boundary conditions at the eddges is violated by the coseismic displacement step associated with periodic slip events. However, the induced bias in interseismic velocity is small provided that the shear zone width is much greater than the seismogenic rupture depth.

For fault geometries and viscoelastic stratification likely to be encountered in practice, the shear zone model generally differs substantially from the conventional model. In particular, for a low-viscosity plastosphere (Maxwell relaxation time short compared with the length of the seismic cycle) the conventional model exhibits large variations in velocity over a single cycle.

This reflects the process of rapid postseismic relaxation early in the cycle versus small relaxation effects late in the cycle, leading to a sharp velocity decrease with time until the cycle is renewed with another earthquake. By contrast, the shear zone model exhibits a more moderate velocity decrease during the cycle because of the stabilizing effect of the shear zone edges. The different responses of these two models are such that inference of the mechanical properties of the schizosphere-plastosphere system such as plastosphere viscosity, elastic plate thickness, depth(s) to onset of steady slip, and slip partitioning among adjacent strike-slip fault strands, may differ substantially according to which model is used to interpret the interseismic velocity pattern. Modeling of the interseismic velocity field around the Mojave segment of the San Andreas fault out to ~200 km distance shows that the conventional model can explain the near-fault portion of the observed velocity field but substantially underpredicts the velocity at distance >50–100 km from the fault. The viscoelastic shear zone model successfully explains both the near-fault and more distant portions of the velocity field, suggesting that lateral variations in viscosity tangibly shape the interseismic velocity field. Assuming that recent observations correspond to a time of four to five tenths into the earthquake cycle, interseismic strain accumulation is characterized as ~50 mm/yr Pacific-North America plate motion being accommodated within a 600-km-wide shear zone which includes the southern San Andreas fault system and Eastern California Shear Zone, with elastic layer thickness of ~15 km, seismogenic layer thickness of 12–15 km, and plastosphere viscosity of 1.6×10^{19} Pa s.

The viscoelastic shear zone model may further provide a framework for evaluating the effect of an external transient change in velocity. Such a change may be driven by postseismic relaxation effects from distant earthquakes outside of the local strike-slip fault system. The given framework can accommodate a sudden or gradual change in the velocities of the shear zone edges as well as the deeper extension(s) of the fault(s) which would accompany the transient change. The short-term consequences of an external perturbation should, according to the behavior revealed here, have a character different from the behavior of the mature fault system, and they could help to clarify the complex response of interacting fault systems.

Appendix A

In order to transform solutions of the laterally homogeneous model (i.e., equations (18) and (23)) into equivalent solutions in the viscoelastic shear zone model, we construct appropriate image solutions of each of the components of the laterally homogeneous model. This is accomplished with the Greens function $G(x;x_0,L,h)$, defined as the response of the viscoelastic system, embedded in the shear zone of width $2L$, to a unit Burgers vector applied at position x_0 ($-L < x_0 < L$) and depth h. This corresponds to substitution of the deformation field $u_0 = \tan^{-1}(x/h)$ into (7) (z-displacement is understood). This leads to

$$G(x;x_0,L,h) = \tan^{-1}\left[\frac{x-x_0}{h}\right] + \sum_{\substack{m=2 \\ \text{even } m}}^{\infty}\left\{\tan^{-1}\left[\frac{x+2Lm-x_0}{h}\right] + \tan^{-1}\left[\frac{x-2Lm-x_0}{h}\right]\right\} + \sum_{\substack{m=1 \\ \text{odd } m}}^{\infty}\left\{\tan^{-1}\left[\frac{x+2Lm+x_0}{h}\right] + \tan^{-1}\left[\frac{x-2Lm+x_0}{h}\right]\right\} - \frac{\pi}{2}\frac{x}{L}$$

$$= G_{\text{even}} + G_{\text{odd}} - \frac{\pi}{2}\frac{x}{L} \qquad (-L < x < L). \tag{A1}$$

The sum of the even m terms in (A1), including the $\tan^{-1}[(x-x_0)/h]$ term, can be evaluated with (B25) of Appendix B. Using the notation of Appendix B, we substitute, for even m,

$$\alpha = \frac{x-x_0}{h}$$
$$\beta = \frac{2L}{h}, \tag{A2}$$

leading to a contribution to G of

$$G_{\text{even}} = \tan^{-1}\left[\coth\frac{\pi h}{4L}\tan\frac{\pi(x-x_0)}{4L}\right]. \tag{A3}$$

Similarly, the sum of the odd m terms in (A1) is obtained from (B24) with

$$\alpha = \frac{x+x_0}{h}$$
$$\beta = \frac{2L}{h}, \tag{A4}$$

leading to a contribution to G of

$$G_{\text{odd}} = \tan^{-1}\left[\tanh\frac{\pi h}{4L}\tan\frac{\pi(x+x_0)}{4L}\right] \tag{A5}$$

This yields

$$G(x;x_0,L,h) = \tan^{-1}\left[\coth\frac{\pi h}{4L}\tan\frac{\pi(x-x_0)}{4L}\right] + \tan^{-1}\left[\tanh\frac{\pi h}{4L}\tan\frac{\pi(x+x_0)}{4L}\right] - \frac{\pi}{2}\frac{x}{L}. \tag{A6}$$

Appendix B

We seek to evaluate the sums

$$I_{\text{odd}} = \sum_{\substack{m=1 \\ \text{odd } m}}^{\infty}\left[\tan^{-1}(\alpha+\beta m) + \tan^{-1}(\alpha-\beta m)\right] \tag{B1}$$

$$I_{\text{even}} = \tan^{-1}(\alpha) + \sum_{\substack{m=2 \\ \text{even } m}}^{\infty}\left[\tan^{-1}(\alpha+\beta m) + \tan^{-1}(\alpha-\beta m)\right] \tag{B2}$$

for real-valued α and β which satisfy $|\alpha/\beta| < 1$ and $\beta > 0$. Differentiation with respect to α yields

$$S_{\text{odd}} = \partial_\alpha I_{\text{odd}} = \sum_{\substack{m=-\infty \\ \text{odd } m}}^{\infty}\frac{1}{1+(\alpha+\beta m)^2} \tag{B3}$$

$$S_{\text{even}} = \partial_\alpha I_{\text{even}} = \sum_{\substack{m=-\infty \\ \text{even } m}}^{\infty}\frac{1}{1+(\alpha+\beta m)^2}. \tag{B4}$$

Note that S_{even} is related to S_{odd} by

$$S_{even}(\alpha,\beta) = S_{odd}(\alpha\pm\beta,\beta) \tag{B5}$$

the + or − sign being chosen such that

$$\left| \frac{\alpha\pm\beta}{\beta} \right| < 1. \tag{B6}$$

Our strategy will thus be to evaluate S_{odd} and S_{even} and then evaluate I_{odd} and I_{even} by integration with respect to α.

Consider the function

$$y(\alpha,\beta,\gamma) = \sum_{\substack{m=1 \\ \text{odd } m}}^{\infty} \frac{e^{\gamma m}}{1 + (\alpha + \beta m)^2} \tag{B7}$$

for $\gamma \le 0$. It is related to S_{odd} by

$$S_{odd} = y(\alpha,\beta,0) + y(-\alpha,\beta,0) \tag{B8}$$

It satisfies the second-order differential equation

$$\partial_{\gamma\gamma}^2 y + 2\alpha\beta^{-1}\partial_\gamma y + \left[\frac{\alpha^2+1}{\beta^2}\right] y = \frac{1}{\beta^2}\frac{e^\gamma}{1-e^{2\gamma}} = R(\gamma). \tag{B9}$$

This has homogeneous solutions

$$\begin{aligned} y_1 &= e^{\beta^{-1}(-\alpha+i)\gamma} \\ y_2 &= e^{\beta^{-1}(-\alpha-i)\gamma} \end{aligned} \tag{B10}$$

With Wronskian

$$W(y_1,y_2) = y_1\,\partial_\gamma y_2 - y_2\,\partial_\gamma y_1 = -2\,i\,\beta^{-1}\,e^{-2\alpha\beta^{-1}\gamma} \tag{B11}$$

a particular solution of (B9) is [*Simmons*, 1972]

$$y = y_1 \int \frac{-y_2\,R(\gamma)}{W(y_1,y_2)}\,d\gamma + y_2 \int \frac{y_1\,R(\gamma)}{W(y_1,y_2)}\,d\gamma. \tag{B12}$$

The general solution of (B9) is the sum of the particular solution (B12) plus a linear combination of the homogeneous solutions y_1 and y_2. From (B7), however, we have that $y(\alpha,\beta,\gamma)$ and $\partial_\gamma y(\alpha,\beta,\gamma)$ tend toward zero as $\gamma \to -\infty$, and therefore (B12) is the required solution. Substituting (B10) and (B11) into (B12) and then (B12) into (B8), we find

$$S_{odd} = -\beta^{-1}\int_{-\infty}^{0}\left[e^{\alpha\beta^{-1}\gamma} + e^{-\alpha\beta^{-1}\gamma}\right]\sin(\beta^{-1}\gamma)\left[\frac{e^\gamma}{1-e^{2\gamma}}\right]d\gamma. \tag{B13}$$

The integrand is symmetric with respect to γ, and therefore

$$S_{odd} = -\frac{\beta^{-1}}{2}\int_{-\infty}^{\infty}\frac{1}{2i}\left[e^{i\beta^{-1}\gamma} - e^{-i\beta^{-1}\gamma}\right] \cdot \left[e^{\alpha\beta^{-1}\gamma} + e^{-\alpha\beta^{-1}\gamma}\right]\frac{e^\gamma}{1-e^{2\gamma}}\,d\gamma. \tag{B14}$$

To evaluate (B14), it suffices to consider the integral

$$I(\alpha) = \int_{-\infty}^{\infty}\frac{1}{2i}\,e^{i\beta^{-1}\gamma}\,e^{\alpha\beta^{-1}\gamma}\,\frac{e^\gamma}{1-e^{2\gamma}}\,d\gamma. \tag{B15}$$

The integration in (B15) may be completed in the upper complex γ plane. Evaluating the contribution of residues at $\gamma = 0, i\pi, 2i\pi$, etc., we obtain

$$\begin{aligned} I(\alpha) &= 2\pi i\left\{\frac{1}{2i}\left[-\frac{1}{4} - \frac{1}{2}\sum_{j=1}^{\infty} e^{\beta^{-1} i\pi j (i+\alpha)}\,e^{i\pi j}\right]\right\} \\ &= -\pi\left[\frac{1}{4} - \frac{1}{2}\frac{e^{i\pi\beta^{-1}(i+\alpha)}}{1+e^{i\pi\beta^{-1}(i+\alpha)}}\right]. \end{aligned} \tag{B16}$$

Twice the real part of $I(\alpha)$ is

$$2\,\mathrm{Re}\,I(\alpha) = \frac{\pi}{2}\left[\frac{-1+e^{-2\pi\beta^{-1}}}{1+e^{-2\pi\beta^{-1}}+2\,e^{-\pi\beta^{-1}}\cos(\pi\beta^{-1}\alpha)}\right]. \tag{B17}$$

Since

$$S_{odd} = -\frac{\beta^{-1}}{2}\left\{2\,\mathrm{Re}\,[I(\alpha) + I(-\alpha)]\right\} \tag{B18}$$

and $2\,\mathrm{Re}\,I(\alpha)$ is symmetric with respect to α, we obtain

$$S_{odd} = \frac{\pi}{2}\beta^{-1}\left[\frac{1-e^{-2\pi\beta^{-1}}}{1+e^{-2\pi\beta^{-1}}+2\,e^{-\pi\beta^{-1}}\cos(\pi\beta^{-1}\alpha)}\right]. \tag{B19}$$

Equation (B5) then yields

$$S_{even} = \frac{\pi}{2}\beta^{-1}\left[\frac{1-e^{-2\pi\beta^{-1}}}{1+e^{-2\pi\beta^{-1}}-2\,e^{-\pi\beta^{-1}}\cos(\pi\beta^{-1}\alpha)}\right]. \tag{B20}$$

We now evaluate

$$I_{odd} = \int_0^\alpha S_{odd}(\alpha,\beta)\,d\alpha. \tag{B21}$$

Defining $r = \pi\beta^{-1}$, $q = e^{-r}$, $u = r\,\alpha$, and $du = r\,d\alpha$ we have

$$I_{odd} = \frac{1}{2}(1-q^2)\int_0^\alpha \frac{1}{(1+q^2)+2\,q\,\cos u}\,du. \tag{B22}$$

The integral in (B22) can be evaluated using [*Abramowitz and Stegun*, 1984, equation 4.3.133]

$$\int \frac{dz}{a+b\cos z} = \frac{2}{(a^2-b^2)^{\frac{1}{2}}}\tan^{-1}\left[\frac{(a-b)\tan\frac{z}{2}}{(a^2-b^2)^{\frac{1}{2}}}\right] \quad (a^2 > b^2), \tag{B23}$$

leading to

$$I_{odd} = \tan^{-1}\left[\tanh\frac{\pi\beta^{-1}}{2}\tan\frac{\pi\beta^{-1}\alpha}{2}\right]. \tag{B24}$$

Similarly, we find from (B20) and (B23) that

$$\begin{aligned} I_{even} &= \int_0^\alpha S_{even}(\alpha,\beta)\,d\alpha \\ &= \tan^{-1}\left[\coth\frac{\pi\beta^{-1}}{2}\tan\frac{\pi\beta^{-1}\alpha}{2}\right]. \end{aligned} \tag{B25}$$

Acknowledgments. I thank Zheng-kang Shen for making available the southern California velocity field analyzed here. Reviews by Roland Bürgmann, William Prescott, Jim Savage, the Associate Editor, and two anonymous reviewers improved the manuscript. This work was partially supported by the Cooperative UC/Los Alamos Research program while the author was a postdoctoral researcher at UC Davis.

References

Abramowitz, M., and I.A. Stegun, *Pocketbook of Mathematical Functions With Formulas, Graphs, and Mathematical Tables*, 468 pp., Natl. Inst. of Stand. and Technol., Gaithersburg, Md., 1984.

Atwater, T., and J. Stock, Pacific-North America plate tectonics of the Neogene southwestern United States: An update, *Int. Geol. Rev.*, *40*, 375-402, 1998.

Brace, W.F., and D.L. Kohlstedt, Limits of lithospheric stress imposed by laboratory experiments, *J. Geophys. Res., 85*, 6348-6252, 1980.

DeMets, C., and T.H. Dixon, New kinematic models for Pacific-North America motion from 3 Ma to present, I: Evidence for steady motion and biases in the NUVEL-1A model, *Geophys. Res. Lett., 26*, 1921-1924, 1999.

Dixon, T.H., M. Miller, F. Farina, H. Wang, and D. Johnson, Present-day motion of the Sierra Nevada block and some tectonic implications for the Basin and Range province, North American Cordillera, *Tectonics, 19*, 1-24, 2000.

Eberhart-Phillips, D., M. Lisowski, and M.D. Zoback, Crustal strain near the big bend of the San Andreas fault: Analysis of the Los Padres-Tehachapi trilateration networks, California, *J. Geophys. Res., 95*, 1139-1153, 1990.

Feigl, K.L., et al., Space geodetic measurement of crustal deformation in central and southern California, 1984-1992, *J. Geophys. Res., 98*, 21,677-21,712, 1993.

Gordon, D., C. Ma, and J.W. Ryan, Results from the mobile VLBI Program in the western United States, in *Contributions of Space Geodesy to Geodynamics: Crustal Dynamics, Geodyn Ser.*, vol 23, edited by D.E. Smith and D.L. Turcotte, pp. 131-138, Washington, D.C., 1993.

Hill, D.P., J.P. Eaton, and L.M. Jones, Seismicity 1980-86, in *The San Andreas Fault System, California*, edited by R.E. Wallace, *U.S. Geol. Surv. Prof. Pap., 1515*, 115-151, 1990.

Humphreys, E.D., and K.G. Dueker, Western U.S. upper mantle structure, *J. Geophys. Res., 99*, 9615-9634, 1994.

Jones, L.M., Focal mechanisms and the state of stress on the San Andreas fault in southern California, *J. Geophys. Res., 93*, 8869-8891, 1988.

Kusznir, N.J., The distribution of stress with depth in the lithosphere; thermorheological and geodynamic constraints, *Philos. Trans. R. Soc. London, Ser A, 337*, 95-110, 1991.

McClusky, S., et al., Global Positioning System constraints on plate kinematics and dynamics in the eastern Mediterranean and Caucasus, *J. Geophys. Res., 105*, 5695-5719, 2000.

Nur, A., and G. Mavko, Postseismic viscoelastic rebound, *Science, 183*, 204-206, 1974.

Pollitz, F.F., Coseismic deformation from earthquake faulting on a layered spherical Earth, *Geophys. J. Int., 125*, 1-14, 1996.

Pollitz, F.F., and I.S. Sacks, Modeling of postseismic relaxation following the great 1857 earthquake, southern California, *Bull. Seismol. Soc. Am., 82*, 454-480, 1992.

Pollitz, F.F., G. Peltzer, and R. Bürgmann, Mobility of continental mantle: Evidence from postseismic geodetic observations following the 1992 Landers earthquake, *J. Geophys. Res., 105*, 8035-8054, 2000.

Roy, M., and L. Royden, Crustal rheology and faulting at strike-slip plate boundaries, 1, An analytic model, *J. Geophys. Res., 105*, 5583-5597, 2000a.

Roy, M., and L. Royden, Crustal rheology and faulting at strike-slip plate boundaries, 2, Effects of lower crustal flow, *J. Geophys. Res., 105*, 5599-5613, 2000b.

Rubin, C.M., and K. Sieh, Long dormancy, low slip rate, and similar slip per event for the Emerson fault, Eastern California Shear Zone, *J. Geophys. Res., 102*, 15,319-15,333, 1997.

Rundle, J.B., Static elastic-gravitational deformation of a layered half space by point couple sources, *J. Geophys. Res., 85*, 5354-5363, 1980.

Sauber, J., W. Thatcher, S.C. Solomon, and M. Lisowski, Geodetic slip rate for the Eastern California Shear Zone and the recurrence time of Mojave Desert earthquakes, *Nature, 367*, 264-266, 1994.

Savage, J.C., Dislocations in seismology, in *Dislocations in Solids*, vol. 3, edited by F.R.N. Nabarro, p. 251-339, North-Holland, New York, 1980.

Savage, J.C., Viscoelastic-coupling model for the earthquake cycle driven from below, *J. Geophys. Res., 105*, 25,525-25,532, 2000.

Savage, J.C., and R.O. Burford, Geodetic determination of relative plate motion in central California, *J. Geophys. Res., 78*, 832-845, 1973.

Savage, J.C., and M. Lisowski, Viscoelastic coupling model of the San Andreas fault along the big bend, southern California, *J. Geophys. Res., 103*, 7281-7292, 1998.

Savage, J.C., M. Lisowski, and W.H. Prescott, An apparent shear zone trending north-northwest across the Mojave desert into Owens valley, eastern California, *Geophys. Res. Lett., 17*, 2113-2116, 1990.

Savage, J.C., and W.H. Prescott, Asthenospheric readjustment and the earthquake cycle, *J. Geophys. Res., 83*, 3369-3376, 1978.

Shen, Z.-K., D.D. Jackson, and B.X. Ge, Crustal deformation across and beyond the Los Angeles basin from geodetic measurements, *J. Geophys. Res., 101*, 27,957-27,980, 1996.

Sieh, K., M. Stuiver, and D. Brillinger, A more precise chronology of earthquakes produced by the San Andreas fault in southern California, *J. Geophys. Res., 94*, 603-623, 1989.

Simmons, G.F., *Differential Equations with Applications and Historical Notes*, 465 pp., McGraw-Hill, New York, 1972.

Trehu, A., Tracing the subducted oceanic crust beneath the central California continental margin: Results from ocean bottom seismometers deployed during the 1986 Pacific Gas and Electric EDGE Experiment, *J. Geophys. Res., 96*, 6493-6506.

Unruh, J., W. R. Lettis, and J. M. Sowers, Kinematic interpretation of the 1992 Landers earthquake, *Bull. Seismol. Soc. Am., 84*, 537-546, 1994.

Wald, D.J., and T.H. Heaton, Spatial and temporal distribution of slip for the 1992 Landers, California, earthquake, *Bull. Seismol. Soc. Am., 84*, 668-691, 1994.

Wason, H.R., and S.J. Singh, Static deformation of a multilayered sphere by internal sources, *Geophys. J. Roy. Astron. Soc., 27*, 1-14, 1972.

Webb, T.H., and H. Kanamori, Earthquake focal mechanisms in the eastern Transverse Ranges and San Emigdio Mountains, southern California and evidence for a decollement, *Bull. Seismol. Soc. Am., 75*, 737-757, 1985.

F. F. Pollitz, U.S. Geological Survey, MS 977, 345 Middlefield Road, Menlo Park, CA 94025. (fpollitz@swave.wr.usgs.gov)

(Received February 10, 2000; revised May 25, 2001;
accepted May 26, 2001.)